FREEDOM: Validated Method for the Rapid Assessment of Incipient Multimodal Faults of Complex Aerospace Systems

Francesco Di Fiore*, Pier Carlo Berri † and Laura Mainini ‡
Politecnico di Torino, Torino, Italy, 10129

Model-based Fault Detection and Isolation (FDI) methods allow to infer the health status of complex aerospace systems through a large quantity of data acquired in-flight, and evaluations of numerical models of the equipment. This results in an intensive computational procedure that can be addressed only grounding the aircraft. We introduce an original methodology to sensitively accelerate FDI by reducing the computational demand to identify the health status of the aircraft. Our scheme FREEDOM – Fast REliability Estimate and incipient fault Detection Of Multiphysics aerospace systems – proposes an original combination of a novel two-step compression strategy to compute offline a synthesized representation of the dynamical response of the system, and uses an inverse Bayesian optimization approach to infer online the level of damage determined by multiple fault modes affecting the equipment. We demonstrate and validate FREEDOM against numerical and physical experiments for the case of an ElectroMechanical Actuator (EMA) employed for secondary flight controls. Particular attention is dedicated to simultaneous incipient mechanical and electrical faults considering different experimental settings. The outcomes validate our FDI strategy, which permits to achieve the accurate identification of complex damages outperforming the computational time of state of the art algorithms by two orders of magnitude.

Nomenclature

$\boldsymbol{A}$	=	DMD informative matrix
$\boldsymbol{B}$	=	set of n_s modes in output from SVD
$\mathscr{D}$	=	dataset of paired damage parameters and noisy observations of the discrepancy function
f	=	noisy observations of the discrepancy function
$\boldsymbol{F}$	=	set of noisy observations of the discrepancy function

*PhD. Student, Department of Mechanical and Aerospace Engineering, francesco.difiore@polito.it, AIAA Member.
†Affiliate, Department of Mechanical and Aerospace Engineering, piercarlo.berri@polito.it, AIAA Member.
‡Visiting/Adjunct Professor, Department of Mechanical and Aerospace Engineering, laura.mainini@polito.it, AIAA Associate Fellow.
Preliminary version presented as Paper 2023-1092 at the AIAA SciTech Forum and Exposition, National Harbor, MD, January 23 - 27, 2023.

i = iteration of the Bayesian scheme for inference

$\boldsymbol{I}$ = stator envelop current

$\boldsymbol{I}_{ref}$ = reference stator envelop current

$\boldsymbol{I}_{mon}$ = monitoring stator envelop current

I_m = current of the electrical motor

k = damage parameter

$\boldsymbol{k}$ = set of damage parameters

$\boldsymbol{k}^*$ = actual damage parameters affecting the system

$\mathscr{K}$ = faults domain

$\boldsymbol{K}$ = Kernel matrix

l = winner neuron

$\mathscr{M}$ = finite-dimensional manifold

n_e = number of measurement locations

n_k = number of damages affecting the system

n_s = number of snapshots

n_w = number of DMD modes

N = number of observations of the discrepancy function

$\mathscr{N}$ = normal distribution

R = resistance of the stator

T_m = torque of the electrical motor

$\boldsymbol{T}$ = SOM training matrix

U = acquisition function

V_m = voltage of the electrical motor

$\boldsymbol{w}_j$ = j-th SOM weight vector

$\boldsymbol{x}$ = measurement locations

$\boldsymbol{y}$ = output signal

$\boldsymbol{y}_M$ = monitoring signal

$\boldsymbol{Y}$ = snapshot matrix

δ = discrepancy function

δ^* = minimum of the discrepancy function

$\boldsymbol{\Delta}$ = set of observations of the discrepancy function

θ_m = angular position of the electrical motor

θ_u = angular position of the aerodynamic surface

κ = covariance function of the Gaussian process surrogate model

λ_i = i-th SVD eigenvalue

μ = mean function of the Gaussian process surrogate model

ν = back-electromotive force coefficient

σ = standard deviation function of the Gaussian process surrogate model

σ_ε = standard deviation of the measurement noise

τ_i = i-th SOM training vector collecting measurement locations $\boldsymbol{x}$ and the n_w DMD modes

υ_i = i-th DMD mode

Υ = set of DMD modes

ϕ = probability density function

Φ = cumulative distribution function

ψ = non-linear dynamical system

ω = angular speed of the electrical motor

I. Introduction

Modern aerospace systems are characterized by a significant level of complexity associated with the demand for high-performance while operating in extreme environments. Those systems are characterized by technological architectures consisting of a variety of heterogeneous subsystems to meet the ever-increasing requirements of superior capabilities. The complexity of aerospace systems further increases with the demand for technological advances to improve the efficiency and environmental sustainability of the next generation aircraft [1]. Indeed, new lower emission solutions for green aviation consist of innovative technologies and equipment that might complicate the overall architecture of systems currently implemented onboard. This growth of technical complexity poses significant challenges in the compliance to reliability requirements: the increasing number of components and physical interactions determine an augmentation of isolated and coupled multimodal failure modes, that would affect the operation of the whole system in hardly predictable ways. The adoption of green technologies further complicates for safety critical applications that require the reliable assessment of incipient damaged condition affecting the system; this permits to anticipate severe faults and support high-regret decision making processes with potentially catastrophic consequences [2]. The difficulties to achieve a reliable identification of complex faults affecting innovative components represent one of the major bottlenecks that contributes to decelerate the adoption of green technologies onboard modern vehicles.

A multitude of approaches have been proposed in literature to address the diagnostics of complex systems [3–5]. Among these, model-based Fault Detection and Isolation (FDI) techniques provide computational approaches to estimate

the health status of complex aerospace systems in presence of multiphysics fault modes. These strategies compute the discrepancy between the output signal measured from the real system with the same signal computed with a numerical model of the system: the current health status is the solution of the identification problem of minimizing the discrepancy between the two signals leading to almost identical responses [6–8]. For example, Dalla Vedova et al. [9] propose an FDI algorithm for the monitoring of electromechanical actuators for aerospace applications, adopting a genetic algorithm to identify the health status of the system minimizing the discrepancy between the current signal computed with a numerical test bench of the actuator and the current obtained with an approximated numerical model of the system. Kolcio [10] develops a model-based autonomous FDI technique where the output signal measured from the system is propagated through a numerical model to detect inconsistencies that allows to diagnose fault modes; this approach has been tested for the monitoring of the attitude control subsystem of a spacecraft. Venkataraman and Seiler [11] use a model-based FDI filter that allows to estimate stuck faults in the split rudder of UAV, comparing the real measurements of the aircraft dynamics and control commands with simulation-based data obtained with a simplified model of the system. Sidhu et al. [12] propose a FDI tecnique for the health monitoring of lithium batteries affected by fault signatures, based on the discrepancy between the measure of the real terminal voltage and the estimated values computed by a Kalman filter.

Model-based FDI algorithms require to measure a signal sensitive to damages with a high acquisition frequency to constitute a reliable indicator of the health condition of the system. This results in a significant amount of data to be stored and processed, and an increased demand for computational resources to address the high dimensionality of the identification problem. Moreover, these approaches rely on a large number of evaluations of expensive numerical models of the system that further raises the hardware resources required to execute the FDI procedure [3]. Safety critical systems introduce further demand for computational capabilities to accurately identify incipient multimodal faults; the FDI task for these systems requires a massive amount of data acquired during flight operations and through the evaluation of expensive numerical models in order to assess incipient damages that would be instead rather difficult to be detected until their effects become severe. Therefore, the FDI procedures are commonly executed grounding the aircraft to leverage adequate hardware resources that are not available onboard. These limitations get in the way of the adoption of new green technologies that might introduce failure modes potentially critical, hindering the path towards sustainable aviation.

This paper proposes an efficient computational framework for fault detection and isolation to accelerate the identification of incipient fault modes in complex aerospace systems, and potentially ease the transition towards the adoption of greener technologies. The goal is to obtain an efficient procedure suitable for the onboard monitoring of innovative technologies. We name and refer to our framework as FREEDOM in the remaining of this paper as the short for Fast REliability Estimate and incipient fault Detection Of Multiphysics aerospace systems. The main features of FREEDOM are: i) a Bayesian scheme for the inference of damages drastically reduces the demand for costly

evaluations of numerical models of the system with a potential efficiency improvement of order of magnitudes; ii) a novel highly informative compression strategy effectively contains the dimensionality of the diagnostics signals while retaining a high-quality informative content; iii) the original combination of these features substantially accelerates the diagnostics procedure: the Bayesian inference leverages the informative compressed signals to accurately identify damage parameters with contained computational resources.

Specifically, the Bayesian routine uses the Gaussian process surrogate model to approximate the discrepancy between the real-world measurements and numerical responses. This predictive framework informs an adaptive sampling scheme realized by the acquisition function that quantifies the utility of querying the fault domain, and directs the computational resources towards the health assessment of the system. The compression strategy relies on the original combination of Dynamic Mode Decomposition (DMD) and Self Organizing Map (SOM). The former extracts the dynamical dominant features of the system, and the latter determines a compressed representation of the first DMD modes. This permits to compute an efficient encoding map that retains only a reduced set of highly informative elements of the original signals for diagnostics processing. By combining efficient compression stages with an effective Bayesian inference step, our novel computational framework FREEDOM rapidly identifies complex and multimodal faults affecting the system, and could be even suitable for onboard computations to monitor the health status of new greener technologies.

The proposed computational framework FREEDOM is demonstrated and validated for the case of an ElectroMechanical Actuator (EMA) employed for the secondary flight control systems of unmanned aerial vehicles or manned civil and military aircraft: EMAs allow to convert electrical power in mechanical handling of the aerodynamic surfaces, and represents an enabling technology towards green electric aviation [13–18]. These systems constitute a challenging benchmark problem for FDI algorithms given the high level of complexity and interaction of multi-physical components, resulting in a multitude of failure modes difficult to predict. We investigate the performance of FREEDOM through numerical experiments involving computer-based models of the EMA system, and validate our framework conducting physical experiments with a test-bench of an EMA developed to implement different failures. In particular, we consider the FDI of small incipient damage conditions involving multiple physical domains and components to emulate a real-world scenario that can be traced in many safety critical applications. We observe the performance of our algorithm over different numerical settings to assess the accuracy and robustness of the FDI procedure. In addition, we validate FREEDOM on a real-world EMA system affected by incipient faults, demonstrating the substantial acceleration of the FDI procedure and potentially enabling the health status monitoring of these systems onboard of aircraft.

This manuscript is organized as follows: Section II introduces the proposed framework FREEDOM, Section III presents the demonstration FDI problem of an electromechanical actuator, Section IV illustrates the experiment setup, Section V discusses the results of our numerical and physical experiments, and Section VI provides concluding remarks.

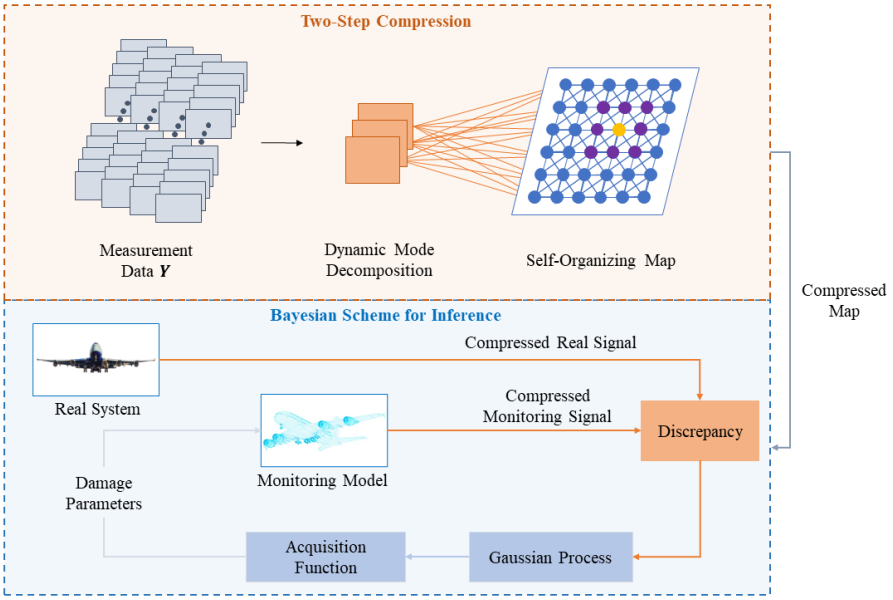

Fig. 1 Schematic representation of the proposed FREEDOM framework.

II. FREEDOM: Methodology and Computational Framework

This paper proposes FREEDOM as a methodology and computational framework for fault detection and isolation to accelerate the identification of incipient fault conditions of complex aerospace systems. Our strategy consists of two main methodological procedures: i) offline we adopt an original two-step compression strategy to compute a synthesized representation of the dynamics of the system reducing the amount of data to be processed during the FDI procedure, and ii) online we implement an inverse Bayesian optimization scheme to accurately identify the health status of the system containing the evaluations of numerical models and computational expense.

The FREEDOM algorithm is schematically described in the diagram of Figure 1. Let us consider a generic complex system characterized by a certain output signal $\boldsymbol{y}(\boldsymbol{k},\boldsymbol{x})$ of n_e elements that is sensitive to the health status of the system $\boldsymbol{k} = \left[k_1,...,k_{n_k}\right]$ defined as a combination of n_k faults modes, and measured in certain locations $\boldsymbol{x}$. In the offline phase, we compute a reference dataset using a scaled Latin Hypercube sampling process [19] to determine a set of n_s incipient health conditions $\boldsymbol{K} = \left[\boldsymbol{k}_1,...,\boldsymbol{k}_{n_s}\right]$ that are used to compute the output signals $\boldsymbol{Y} = \left[\boldsymbol{y}_0(\boldsymbol{k}_0,\boldsymbol{x}),...,\boldsymbol{y}_{n_s}(\boldsymbol{k}_{n_s},\boldsymbol{x})\right]$. The dataset $\boldsymbol{Y}$ is obtained by evaluating a high-fidelity accurate model or through a real-world test bench, and is considered the ground truth reference data of the system. These information are usually high-dimensional and demand for intensive computations to be stored and processed during FDI. Therefore, we propose an original two-step signal compression based on two projection methods to determine a synthesized representation of the signal $\hat{\boldsymbol{y}}(\boldsymbol{k},\hat{\boldsymbol{x}})$ and retain only the highly informative $n_w << n_e$ data.

Online, we perform the fault detection and isolation task to identify the current health status of the system – specified by the combination of fault parameters $\boldsymbol{k}$. The proposed FDI algorithm is based on a Bayesian scheme for inversion to

infer the health status of the system by minimizing the discrepancy between the output signal of the real system and the signal computed with a fast monitoring model. In this stage, we use the compressed informative map $(\hat{\boldsymbol{x}},\hat{\boldsymbol{y}})$ to place measurement points and reduce the dimension of the output signal. To solve this identification problem, our inverse Bayesian technique approximates the discrepancy between the real and numerical output through a Gaussian process surrogate model progressively updated by an acquisition function, that selects the next promising combination of faults to be evaluated.

The following Sections describe in detail the two main elements that characterize FREEDOM. Specifically, Section II.A deals with the original two steps signal compression strategy, and Section II.B illustrates the FDI procedure adopting the Bayesian scheme for inference.

A. Two-Step Compression Strategy

In most aerospace applications, the output signal $\boldsymbol{y}$ needs to be measured with a high acquisition frequency that results in n_e measurements in the order of several thousands to capture all the required amount of information with a satisfactory level of accuracy. This determines the high-dimensionality of the output signal $\boldsymbol{y}$, and represents a significant challenge to rapidly assess the health status of the system due to the demand for large storage capabilities and processing power.

To address this issue, we propose a novel compression strategy to contain the dimensionality of the output signal $\boldsymbol{y}$, and retain only $n_w << n_e$ measurement locations to store and process for the FDI procedure. Our approach identifies the most informative elements n_w of the output signal $\boldsymbol{y}$ through a two-step compression method; First, dynamic mode decomposition extracts a set of dominant coherent structures of the system. Then, a self organizing map computes a compressed representation of the output signal $\boldsymbol{y}$ to retain the highly informative elements that effectively synthesize the dynamic of the system. This procedure is inspired by the compression strategy proposed by Mainini and Willcox [20, 21], where Proper Orthogonal Decomposition (POD) and Self Organizing Maps (SOM) are jointly adopted to determine the optimal placement of sensors for the assessment of structural health status. Berri et al [19] use a similar approach in which POD and SOM are combined to reduce the computational burden associated with the storage of the output signal of actuation systems for aerospace applications.

1. Extracting the Dynamic Features of the System

The first step of our compression strategy leverages the Dynamic Mode Decomposition (DMD) technique to identify the inherent structure of the high-dimensional output signal, extract its the dynamical features, and define a data-driven reduced order representation of the system [22, 23]. DMD has been successfully employed in aerospace engineering applications to compute the modes and associated frequency of complex dynamical systems from large physics-based datasets. Zhao et al. [24] adopt the DMD technique to analyze the physical features of the flow around an airfoil with

leading-edge protuberance considering a stall regime. Cartocci et al. [25] develop a data-driven approach to model the attitude dynamics of a CubeSat satellite using a DMD algorithm, computing fast low-dimensional representations that are used to control the attitude of the system. Deem et al. [26] propose a framework based on a linear quadratic regulator to control a separated laminar boundary layer, where DMD is adopted online to provide a lower-dimensional representation of the space-time evolution of the controlled flow field.

Considering a generic non-linear dynamical system ψ acting on a finite-dimensional manifold $\mathscr{M}$, DMD computes a matrix $\boldsymbol{A}$ whose spectrum provides an approximation of the spectrum of an infinite-dimensional linear Koopman operator that encodes ψ. This allows to derive the dynamical properties of the non-linear system as the dominant eigenvalues and eigenvectors of the informative matrix $\boldsymbol{A}$. We are interested in a non-linear dynamical system $\psi : \mathscr{M} \rightarrow \mathscr{M}$ characterized by the output signal $\boldsymbol{y}(\boldsymbol{k},\boldsymbol{x}) : \mathscr{M} \rightarrow \mathbb{R}$ dependent on the health status of the system $\boldsymbol{k}$ and on measurement locations $\boldsymbol{x}$. Following the DMD approach, we assume that a set of pairs n_s observations $\tilde{\boldsymbol{y}}(\boldsymbol{k}_{j-1},\boldsymbol{x})$ and $\tilde{\boldsymbol{y}}(\boldsymbol{k}_j,\boldsymbol{x})$ are available for different health conditions $\boldsymbol{k}_j$ with $j = 1,2,...,n_s$. We use a scaled Latin hypercube sampling process [19] to collect the n_s incipient faults condition $\boldsymbol{k}$ from the space of possible faults $\boldsymbol{K} = \left[\boldsymbol{k}_0,...,\boldsymbol{k}_{n_s}\right]$ that are used to compute the output signals from the dynamical system. DMD seeks to determine the matrix $\tilde{\boldsymbol{A}} \in \mathbb{R}^{n_e \times n_e}$ such that:

$$\tilde{\boldsymbol{A}}\tilde{\boldsymbol{Y}} = \tilde{\boldsymbol{Y}}' \tag{1}$$

where the matrices $\tilde{\boldsymbol{Y}} = \left[\tilde{\boldsymbol{y}}(\boldsymbol{k}_0,\boldsymbol{x}) \quad \tilde{\boldsymbol{y}}(\boldsymbol{k}_1,\boldsymbol{x}) \quad ... \quad \tilde{\boldsymbol{y}}(\boldsymbol{k}_{n_s-1},\boldsymbol{x})\right] \in \mathbb{R}^{n_e \times n_s}$ and $\tilde{\boldsymbol{Y}}' = \left[\tilde{\boldsymbol{y}}(\boldsymbol{k}_1,\boldsymbol{x}) \quad \tilde{\boldsymbol{y}}(\boldsymbol{k}_2,\boldsymbol{x}) \quad ... \quad \tilde{\boldsymbol{y}}(\boldsymbol{k}_{n_s},\boldsymbol{x})\right] \in \mathbb{R}^{n_e \times n_s}$ are assembled using the series of output signals computed for different health conditions. In real world applications, the matrix $\tilde{\boldsymbol{A}}$ may be extremely large due to the high-dimensionality of $\boldsymbol{y}$ making intractable the direct solution of Equation (1). A popular approach to mitigate these difficulties is to reduce the spatial dimension of the matrices $\tilde{\boldsymbol{Y}}$ and $\tilde{\boldsymbol{Y}}'$ using Singular Value Decomposition (SVD) [27]. The main output of SVD is a set of n_s modes $\boldsymbol{B} \in \mathbb{C}^{n_e \times n_s}$ that represent a low-order representation of $\mathbb{R}^{n_e}$. We employ only the first modes $n_w << n_s$ according to the fraction of information retained from the original observation computed as the cumulative sum $\sum_{i=1}^{n_w} \lambda_i / \sum_{i=1}^{n_s} \lambda_i$ of the eigenvalues λ associated to the considered modes. This allows to define the matrices $\boldsymbol{Y}$ and $\boldsymbol{Y}'$ as the projection of $\tilde{\boldsymbol{Y}}$ and $\tilde{\boldsymbol{Y}}'$ onto the first n_w modes as follows:

$$\boldsymbol{Y} = \boldsymbol{B}^*\tilde{\boldsymbol{Y}} \in \mathbb{R}^{n_w \times n_s} \ , \quad \boldsymbol{Y}' = \boldsymbol{B}^*\tilde{\boldsymbol{Y}}' \in \mathbb{R}^{n_w \times n_s} \tag{2}$$

where $\boldsymbol{B}^*$ is the Hermitian transpose of $\boldsymbol{B}$. Combining Equation (1) and Equation (2), the DMD problem is reduced in the form:

$$\boldsymbol{A} = \boldsymbol{Y}'\boldsymbol{Y}^+ \tag{3}$$

where $\boldsymbol{Y}^{+}$ is the Moore-Penrose pseudoinverse of $\boldsymbol{Y}$. Through the DMD technique, we obtain a set of dynamic modes $\boldsymbol{\Upsilon} = [\boldsymbol{\upsilon}_1, ..., \boldsymbol{\upsilon}_{n_w}]$ corresponding to the dominant eigenvectors of $\boldsymbol{A}$ that are employed in the following step of the compression procedure to identify the most informative locations of the output signal $\boldsymbol{y}$.

2. Projecting to a Lower-Dimensional Space

The second step of the proposed compression strategy determines a synthetized representation of the output signal $\hat{\boldsymbol{y}}(\boldsymbol{k}, \hat{\boldsymbol{x}})$ through a Self Organizing Maps (SOM) identifying only the highly informative $n_w << n_e$ elements of $\boldsymbol{y}$ to be stored and processed for fault detection and isolation.

Self Organizing Maps are a class of single-layer neural networks that identifies clusters of self-similar data through unsupervised competitive learning strategies [28, 29]. SOM maps a high-dimensional space into a lower-dimensional space represented as a two-dimensional grid of nodes initialized as a randomly generated weight vector. Each of the neurons of the SOM has two representations: the first is the space of the weight vectors that are updated during the training process, and the second representation is the fixed bi-dimensional topological space of the network. SOMs have been adopted for various classes of applications, including the improvement of sensors capabilities for prognostics considering different operational regimes in turbofan engines for aerospace applications [30], and the faults detection and prognostics of electrical components [31] and bearings [32] for industrial applications.

For the specific complex systems considered in this work, we define the training set $\boldsymbol{T}$ consisting of the dynamic modes computed through the DMD procedure illustrated in Section II.A.1 and the associated measuring locations $\boldsymbol{x}$:

$$\boldsymbol{T} = [\boldsymbol{x}, \boldsymbol{\upsilon}_1, ..., \boldsymbol{\upsilon}_{n_w}] \tag{4}$$

Each row $\boldsymbol{\tau}_i$ of $\boldsymbol{T}$ represents a training point that is fed to the network during the training process, and the winner neuron l is chosen as the one that minimizes the distance between the associated weight vector $\boldsymbol{w}_l$ and the current training point $\boldsymbol{\tau}_i$:

$$l = \arg\min_j \left(||\boldsymbol{\tau}_i - \boldsymbol{w}_j|| \right) \tag{5}$$

where $||\cdot||$ denotes the L2 norm. At this point, the weight vector of the winner neuron and its neighbors are updated through a neighbourhood function, and the process iterates until all the training points are administered to the network for several epochs where their order is differently randomized.

After the training procedure, we obtain an efficient compression mask $\hat{\boldsymbol{y}}$ of the output signal $\boldsymbol{y}$ leveraging the property that the weight vectors of the trained SOM represent a non linear projection of the high-dimensional training set $\boldsymbol{T}$ to the lower dimensional space of the neurons [20, 21, 33]. As a consequence, the weight vectors defined in the space of the input encode representative vectors for clusters of self-similar points. This permits to define $\hat{\boldsymbol{y}}$ from the components of

the weight vectors associated with the locations $\boldsymbol{x}$ measuring the output signal $\boldsymbol{y}$ only in the n_w informative locations $\hat{\boldsymbol{x}}$. At this point, the compression mask $\hat{\boldsymbol{y}}(\boldsymbol{k},\hat{\boldsymbol{x}})$ consists of n_w highly informative measurements of the output signal that is used online to reduce the dimensionality of the diagnostics procedure.

B. Inverse Bayesian Fault Detection and Isolation

The proposed FDI strategy accelerates the identification of the system health status through an effective use of data from numerical models, and the adoption of the highly informative compressed representation of the signals. The FDI task represents an inverse problem where the identification of the fault parameters affecting the system is performed through optimization strategies that usually rely on gradient-based or meta-heuristic algorithms [3]; those approaches require a large number of data from numerical models or test-benches of the system, which makes the computational cost unfeasible for the onboard health monitoring.

To overcome this issues, we propose an FDI algorithm based on an inverse Bayesian optimization approach that wisely uses a limited amount of data from the monitoring model of the system to contain the computational cost required for the identification task. Bayesian optimization (BO) is a well-established machine learning strategy for the global optimization of noisy, expensive-to-evaluate black-box objective functions [34–37]. The term black-box refers to functions whose analytical form is not available or the derivatives are not accessible; this is the case of objective functions that depends on the dynamic of a system evaluated through a numerical model or a physical test bench that can be depicted in terms of input/output relationship. Bayesian optimization has been widely employed for design and optimization of aerospace systems from wings for supersonic transport aircraft [38] to laminated composites for aerospace structures [39], and for the multidisciplinary design optimization of complete aircraft [40] and partially reusable launch vehicles [41].

In the context of FDI, we aim to infer the combination of fault parameters $\boldsymbol{k}^*$ that minimizes the discrepancy δ between the output signal $\boldsymbol{y}(\boldsymbol{k}^*,\boldsymbol{x})$ measured in the locations $\boldsymbol{x}$ from the physical system and the same signal $\boldsymbol{y}_M(\boldsymbol{k},\boldsymbol{x})$ computed with a numerical model. This problem may be challenging to be solved with a contained computational cost since the output signals $\boldsymbol{y}$ and $\boldsymbol{y}_M$ encode a significant number of measurements. To reduce the dimensionality of the problem, we leverage the compression mask $\hat{\boldsymbol{y}}(\boldsymbol{k},\hat{\boldsymbol{x}})$ computed with our two-step compression strategy and formalize the FDI task as follows:

$$\boldsymbol{k}^* = \underset{\boldsymbol{k}\in\mathscr{K}}{\arg\min}\, \delta(\boldsymbol{k},\hat{\boldsymbol{x}}) \tag{6}$$

where $\delta(\boldsymbol{k},\hat{\boldsymbol{x}}) = ||\hat{\boldsymbol{y}}(\boldsymbol{k}^*,\hat{\boldsymbol{x}}) - \hat{\boldsymbol{y}_M}(\boldsymbol{k},\hat{\boldsymbol{x}})||$.

To solve Equation (6), BO adopts two elements: a Bayesian surrogate model to approximate the discrepancy δ, and an acquisition function to select the next fault combination to be evaluated. Algorithm 1 illustrates the main steps of the

Algorithm 1 Bayesian scheme for the inference of damage parameters

Input: Definition of the faults domain $\mathscr{K} \in \mathbb{R}^{n_k}$, discrepancy function $\delta(\boldsymbol{k},\hat{\boldsymbol{x}})$ and the Gaussian process surrogate model prior $GP(0,\kappa(\boldsymbol{k},\boldsymbol{k}'))$

Output: Actual damage configuration affecting the system $\boldsymbol{k}^* = \arg\min \delta(\boldsymbol{k},\hat{\boldsymbol{x}})$

$\mathscr{D}_0 \leftarrow \{\boldsymbol{k}_n, f(\boldsymbol{k}_n)\}_{n=1}^{N_0}$ collect initial N_0 noisy observations of the discrepancy function $f(\boldsymbol{k}_n) \sim \mathscr{N}(\delta(\boldsymbol{k}_n,\hat{\boldsymbol{x}}),\sigma_\varepsilon)$

$\mu_0, \sigma_0 \leftarrow$ compute the initial mean and standard deviation of the Gaussian process surrogate model

$i \leftarrow 1$

repeat

  Load the new combination of damage parameters $\boldsymbol{k}_{N_i}$

  Compute the observation of the discrepancy function $f(\boldsymbol{k}_{N_i})$

  $\mathscr{D}_i \leftarrow \mathscr{D}_{i-1} \cup \{\boldsymbol{k}_{N_i}, f(\boldsymbol{k}_{N_i})\}$ update the dataset of observations

  $\mu_i, \sigma_i \leftarrow$ update the mean and standard deviation of the Gaussian process surrogate model

  Compute the acquisition function $U(\boldsymbol{k} \mid \mathscr{D}_i)$ on the updated dataset $\mathscr{D}_i$

  Maximize the acquisition function to select the next damage configuration to query $\boldsymbol{k}_{N_{i+1}} = \max_{\boldsymbol{k}\in\mathscr{K}} U(\boldsymbol{k} \mid \mathscr{D}_i)$

  $i+1 \leftarrow i$

until Convergence criteria is met

return Combination of damage parameters $\boldsymbol{k}^*$ that minimizes the discrepancy function $\delta(\boldsymbol{k}_n,\hat{\boldsymbol{x}})$ over the faults domain $\mathscr{K}$

inverse Bayesian FDI framework. BO sequentially collects noisy observations of δ and learns a probabilistic surrogate model to quantify the current belief about the discrepancy between the response of the real system and the outcome of the monitoring model. This statistical model is typically a Gaussian process due to their flexibility, analytic properties and well-calibrated uncertainty [42, 43]. We discuss the Bayesian statistical modeling using Gaussian processes in Section II.B.1. At this point, the acquisition function uses the surrogate information to measure the utility of making any given evaluation of δ. In Section II.B.2, we discuss popular acquisition functions including the expeceted improvement, upper confidence bound, and two-step lookahead expected improvement. The process iterates until a maximum number of evaluations of the monitoring model are reached to contain the total computational expense. We now provide details about the main components of the inverse Bayesian fault detection and isolation framework, first discussing the Gaussian process regression (Section II.B.1) and then illustrating different formulations of the acquisition function (Section II.B.2)

1. Gaussian Process Regression

Gaussian process (GP) regression is a flexible and efficient framework to approximate the discrepancy δ through a non-parametric kernel-based statistical model [42, 43]. GP allows to predict the values of the discrepancy across the domain $\mathscr{K}$ based on its observations at previous evaluated points, and quantifies the uncertainty associated with the prediction. In the following, we briefly summarize the theoretical formulation of GP.

Let $\mathscr{D}_N = \{\boldsymbol{k}_n, f(\boldsymbol{k}_n)\}_{n=1}^N$ denote the dataset of N paired health conditions $\boldsymbol{k}_n \in \mathscr{K} \subseteq \mathbb{R}^{n_k}$ and noisy observations of the discrepancy $f(\boldsymbol{k}_n) \sim \mathscr{N}(\delta(\boldsymbol{k}_n,\hat{\boldsymbol{x}}),\sigma_\varepsilon)$, where σ_ε is the standard deviation of the normally distributed noise. GP is a non parametric model characterized by its mean function $\mu(\boldsymbol{k}) : \mathscr{K} \to \mathbb{R}$ and the covariance function also defined as kernel function $\kappa(\boldsymbol{k},\boldsymbol{k}') : \mathscr{K} \times \mathscr{K} \to \mathbb{R}$. We assume that the observations of the objective function $\boldsymbol{\Delta} = \{\delta_n\}_{n=1}^N$ are jointly Gaussian, and the output $\boldsymbol{F} = \{f(\boldsymbol{k}_n)\}_{n=1}^N$ is normally distributed given δ:

$$\boldsymbol{\Delta} \mid \boldsymbol{k} \sim \mathscr{N}(\boldsymbol{\mu}, \boldsymbol{K}) \tag{7}$$

$$\boldsymbol{F} \mid \boldsymbol{\Delta}, \sigma_{\varepsilon}^2 \sim \mathscr{N}(\boldsymbol{\Delta}, \sigma_{\varepsilon}^2 \boldsymbol{I}) \tag{8}$$

where $\mu := \mu(\boldsymbol{k}_n)$, and $K_{i,j} =: \kappa(\boldsymbol{k}_i, \boldsymbol{k}_j)$.

Using the Bayesian inference principle, the GP regression combines the prior belief about the objective $p(\delta)$ with the likelihood function $p(\mathscr{D}_N|\delta)$ to compute the posterior distribution $p(\delta|\mathscr{D}_N) \propto P(\mathscr{D}_N|\delta)P(\delta)$, representing the updated surrogate model of the objective function. Assuming the prior of the objective as a GP: $\delta \sim GP(0, \kappa(\boldsymbol{k}, \boldsymbol{k}'))$ with zero mean function $\mu(\boldsymbol{k}) = 0$, the posterior distribution is a GP completely defined by its mean μ and variance σ^2:

$$\mu(\boldsymbol{k}) = \kappa_i(\boldsymbol{k})^T \left(\boldsymbol{K} + \sigma_{\varepsilon} \boldsymbol{I}\right)^{-1} \boldsymbol{F} \tag{9}$$

$$\sigma^2(\boldsymbol{k}) = \kappa(\boldsymbol{k}, \boldsymbol{k}) - \kappa_i(\boldsymbol{k})^T \left(\boldsymbol{K} + \sigma_{\varepsilon} \boldsymbol{I}\right)^{-1} \kappa_i(\boldsymbol{k}) \tag{10}$$

where κ_i is defined as $\kappa_i(\boldsymbol{k}) \doteq \big(\kappa(\boldsymbol{k}, \boldsymbol{k}_0), \cdots, \kappa(\boldsymbol{k}, \boldsymbol{k}_i)\big)$. The posterior mean μ represents the maximum a posteriori probability estimate of the discrepancy δ, and the posterior standard deviation σ quantifies the uncertainty of the surrogate model. These information are used to compute the acquisition function that guides the search towards the optimal solution of the optimization problem in Equation (6).

In addition, the estimate of the uncertainty σ associated with the prediction μ of the discrepancy through the kernel function κ represents a significant property that potentially confers our FDI framework a form of intrinsic reliability. Indeed, kernel functions form a reproducing kernel Hilbert space in which the discrepancy δ has bounded norm [44, 45]. This provides reliable confidence intervals on the discrepancy that determine a measure of the prediction and therefore reliability of the Gaussian process surrogate model. In our case, this would pave the way for robust inference of the health status of the system.

2. Acquisition Function

Given the surrogate model of the discrepancy δ, it is possible to define an acquisition function $U(\boldsymbol{k}) : \mathscr{K} \to \mathbb{R}^+$ under the GP posterior that quantifies the improvement of the solution of the FDI problem (Equation 6) once the discrepancy is evaluated at a new set of fault parameters. At each iteration of the FDI process, BO selects the most promising combination of fault parameters $\boldsymbol{k}_{N+1}$ to be evaluated in the next iteration by maximizing the acquisition function:

$$\boldsymbol{k}_{N+1} = \underset{\boldsymbol{k}\in\mathscr{K}}{\arg\max}\, U(\boldsymbol{k} \mid \mathscr{D}_N) \tag{11}$$

Once the new health condition is computed, BO evaluates the value of the discrepancy $\delta(\boldsymbol{k}_{N+1},\hat{\boldsymbol{x}})$ and uses this information to expand the dataset $\mathscr{D}_{N+1}$; as the dataset has been extended, the GP posterior is updated and the acquisition function evolves through the optimization.

In this paper, we discuss and investigate the performance of three popular formulations of the acquisition function for the fault detection and isolation task, including the expected improvement (EI), upper-confidence bound (UCB), and two-step lookahead expected improvement (2lookEI). These acquisition functions are designed to address a trade-off between the exploration of the faults space $\mathscr{K}$ to reduce the uncertainty of the GP model, and the exploitation of the most promising regions of $\mathscr{K}$ where the minimum value of the discrepancy is likely to be located. The rationale behind the selection of these specific acquisition functions is to investigate different approaches to measure the improvement of the solution in terms of identification of the health status of the system. In the following, we review and discuss the formulations of EI, UCB and 2lookEI.

Expected Improvement

The expected improvement (EI) acquisition function measures the improvement in the estimate of the health status of the system as the expected probability that a certain health condition leads to a reduction of the best value of discrepancy observed so far. Given the posterior mean $\mu(\boldsymbol{k})$ (Equation (9)) and the standard deviation $\sigma(\boldsymbol{k})$ (Equation (10)) of the Gaussian process model, the Expected Improvement is defined as follows [46]:

$$U_{EI}(\boldsymbol{k}) = \begin{cases} \left(\mu(\boldsymbol{k}) - \delta(\boldsymbol{k}^+)\right)\Phi(Z) + \sigma(\boldsymbol{k})\phi(Z) & \text{if} \quad \sigma(\boldsymbol{k}) > 0 \\ 0 & \text{if} \quad \sigma(\boldsymbol{k}) = 0 \end{cases} \tag{12}$$

where $\delta(\boldsymbol{k}^+)$ is the value of the discrepancy evaluated at the health condition $\boldsymbol{k}^+$ determined so far that realizes the larger reduction of δ, Φ is the cumulative distribution function, ϕ is the probability density function of the standard normal distribution, and $Z = \left(\mu(\boldsymbol{k}) - \delta(\boldsymbol{k}^+)\right)/\sigma(\boldsymbol{k})$ is the standardized improvement.

Upper-Confidence Bound

The upper confidence bound (UCB) acquisition function defines an optimistic selection strategy of favourable health conditions of the system under-estimating the prediction of the Gaussian process with added uncertainty. In the context of minimizing δ, UCB uses the lower confidence for every health status corresponding to effectively using a fixed probability best case scenario according to the Gaussian process model. The formulation of UCB is a weighted sum of

the mean function $\mu(\boldsymbol{k})$ (Equation (9)) and the uncertainty $\sigma(\boldsymbol{k})$ (Equation (10)) [47]:

$$U_{UCB}(\boldsymbol{k}) = \mu(\boldsymbol{k}) - \sqrt{\beta_n}\sigma(\boldsymbol{k}) \tag{13}$$

where $\sqrt{\beta_n} = 1/(\sqrt{2n^2\pi^2})$ is the weight defined as a function of the number of evaluations n of the discrepancy δ.

Two-Step Lookahead Expected Improvement

The two-step lookahead expected improvement (2lookEI) quantifies the current informative gains given by a potential health condition of the system, and uses this data to determine a new health status on the next query that produces larger reduction of the discrepancy δ. This is obtained through an optimal sampling policy to determine the health condition $\boldsymbol{k}$ at the second future iteration of the optimization that maximizes the cumulative expected improvement (Equation 12) over two iterations [48]:

$$U_{2lookEI}(\boldsymbol{k}^{(2)}) = U_{EI}^{(0)}(\boldsymbol{k}^{(1)}) + \mathbb{E}^{(0)}\left[max_{\boldsymbol{k}^{(2)}\in\mathscr{K}} U_{EI}^{(1)}(\boldsymbol{k}^{(2)})\right] \tag{14}$$

where the apex 0 refers to the elements computed at the current iteration of the FDI procedure, and 1 and 2 define variables evaluated at the first and second future iteration, respectively. Equation (14) is not computable in closed form as it requires the evaluation of the nested expectation and maximization term. In particular, the second term of $U_{2lookEI}$ has to be assessed evaluating Equation 12 through the Gaussian process updated at the first future iteration, which is not directly available at the current iteration of the FDI procedure. To overcome this issue, we adopt a Monte Carlo approach to provide a reliable approximation of $U_{2lookEI}$ through the estimate of the mean $\mu^{(1)}$ and standard deviation $\sigma^{(1)}$ of the GP model at the first future iteration [49]:

$$\mu^{(1)}(\boldsymbol{k}) = \mu^{(0)}(\boldsymbol{k}) + \boldsymbol{H}^{(0)}\left(\boldsymbol{k}\right) Z \tag{15}$$

$$\sigma^{(1)}(\boldsymbol{k}) = \sigma^{(0)}(\boldsymbol{k}) - \boldsymbol{H}^{(0)}\left(\boldsymbol{k}\right)\boldsymbol{H}^{(0)}\left(\boldsymbol{k}\right)^T \tag{16}$$

where Z is an independent standard normal random variable, $\boldsymbol{H}^{(0)}\left(\boldsymbol{k}\right) = \kappa^{(0)}\left(\boldsymbol{k}\right)\boldsymbol{C}^{(0)}(\boldsymbol{k})^{-1}$, C is the Cholesky decomposition of the covariance matrix $\kappa(\boldsymbol{k}_i,\boldsymbol{k}_j)$. To estimate $U_{2lookEI}$, we sample the random variable Z and compute $U_{EI}^{(1)}$ combining Equation 15 and Equation 16: averaging over many Z provides a robust estimate of the two-step lookahead expected improvement.

fault parameter	fault mode	$k_i = 0$ (no damage)	$k_i = 1$ (full damage)
k_1	friction	nominal	3 times nominal
k_2	backlash	nominal	100 times nominal
k_3	phase A short circuit	absent	complete
k_4	phase B short circuit	absent	complete
k_5	phase C short circuit	absent	complete
k_6	rotor eccentricity	absent	air gap width
k_7	eccentricity phase	-180°	180°

Table 1 Definition of the health status of the EMA system in terms of fault parameters k_i

III. Fault Detection and Isolation: Problem Setup

Without losing the generalization properties of our method, we demonstrate and validate the computational framework FREEDOM for the FDI problem of an ElectroMechanical Actuator (EMA) adopted for the flight control system of manned aircraft. EMAs represent a complex multiphysics system that constitute a potential enabling technology for sustainable aviation according to the more electric and all electric aircraft philosophies: these systems permits the elimination of a centralized hydraulic power generation system with benefits in terms of lower emissions and weight reduction [13–18]. EMAs constitute a significant challenge for the FDI procedure due to the presence of different subsystems characterized by heterogeneous and coupled physical domains. The EMAs architecture consists of an electrical power unit coupled with a mechanical transmission that converts the electric power from the aircraft electrical system into mechanical power to control the aerodynamic surfaces. For the specific EMA considered in this work, the electrical power unit consists of three elements: i) the actuator control electronic compares the position setpoint required by the user with the actual position and speed of the aerodynamic surface to define a torque setpoint for the electrical motor through a control law; ii) the three phase inverter controls the electric motor phase commutation sequence, and feeds to the motor the required voltages of the motor coils; iii) the electric motor provides the required torque necessary to move the flight control surfaces. This torque is transmitted through the gearbox of the mechanical transmission to the aerodynamic surfaces, and counteracts the aerodynamic hinge moment acting on the actuator to move the flight controls at the prescribed position and speed.

In this paper, we consider 4 different failure modes affecting the EMA system, including the increase of friction (k_1) and backlash (k_2) of the mechanical transmission, partial short circuit for the three phases of the electrical motor (k_3, k_4, k_5), and the static eccentricity of the rotor (k_6, k_7). This results in the health status of the system $\boldsymbol{k} = \left[k_1, k_2, k_3, k_4, k_5, k_6, k_7\right]$ defined as a combination of $n_k = 7$ elements. Table 1 summarizes the fault modes affecting the considered EMA system; these failure conditions are selected among the most common EMA faults during the in-flight operations [50, 51]. Each fault parameter $k_i \in [0, 1]$ is normalized between 0 and 1, where $k_i = 0$ represents the nominal condition and $k_i = 1$ indicates the complete damaged condition. We consider as incipient damages values

of fault parameters $k_i < 0.05$ which represent a condition where the system is still capable to meet the operational requirements with a small degradation of the performance.

For the FDI procedure illustrated in Section II, we adopt the stator envelop current $\boldsymbol{I}$ of the electrical motor as the output signal of the system to determine its health status: this signal is sensitive to the failure modes considered in this study and is easy to be acquired in a real-word physical system [19, 52]. Thus, the FDI problem of the considered aerospace EMA is formulated according to Equation (6) as follows:

$$\boldsymbol{k}^* = \underset{\boldsymbol{k}\in\mathscr{K}}{\arg\min} ||\hat{\boldsymbol{I}_{ref}}(\boldsymbol{k}^*,\hat{\boldsymbol{x}}) - \hat{\boldsymbol{I}_{mon}}(\boldsymbol{k},\hat{\boldsymbol{x}})|| \tag{17}$$

where $\boldsymbol{k} = [k_1,...,k_7]$ represents the health status of the considered system, and $\mathscr{K} = \left[0,1\right]^7$ is the space of the fault parameters. To solve this FDI task, we use offline a high-fidelity computer-based model of the EMA system (Section III.A.1) as the source of the reference dataset that is used to compute the compression mask $\hat{\boldsymbol{I}}(\boldsymbol{k}^*,\hat{\boldsymbol{x}})$ through the proposed two-step compression strategy (Section II.A). During the online phase, we adopt the inverse Bayesian approach for FDI (Section II.B) to compute the health status of the system; we use both a high-fidelity numerical model and a real-world test bench of the EMA system to provide the reference current signal $\boldsymbol{I}_{ref}$, and a simplified low-fidelity numerical model to evaluate the monitoring current signal $\boldsymbol{I}_{mon}$ with a contained computational cost.

In the following, we present the numerical high-fidelity model of the EMA system in Section III.A.1, and the approximated low-fidelity monitoring model in Section III.A.2. We then illustrate the experimental test-bench of the EMA in Section III.B.

A. Computer-Based Physical Models of the System

In this paper, we consider two computer-based models of the EMA system at different levels of accuracy and computational cost. The high-fidelity model (Section III.A.1) is used in the offline phase as the source of information to build the reference dataset for the two-step compression strategy, and online as the emulator of the real EMA to compute the reference current signal that is adopted during the Bayesian FDI procedure. This model provides an accurate representation of the dynamic of the system considering both the nominal and damaged condition, but requires a significant computational cost that is not suitable for an efficient health monitoring procedure. To overcome this issue, the low-fidelity numerical model of the EMA (Section III.A.2) provides a less accurate estimate of the response of the system that can be used online as the source of data to compute the monitoring signal, given the contained computational resources required for its evaluation.

1. High-Fidelity Reference Model

The high-fidelity model of the EMA system is a highly accurate physics-based numerical model that is capable to emulate the dynamical response of the actuator, and has been validated against experimental data [52–54].

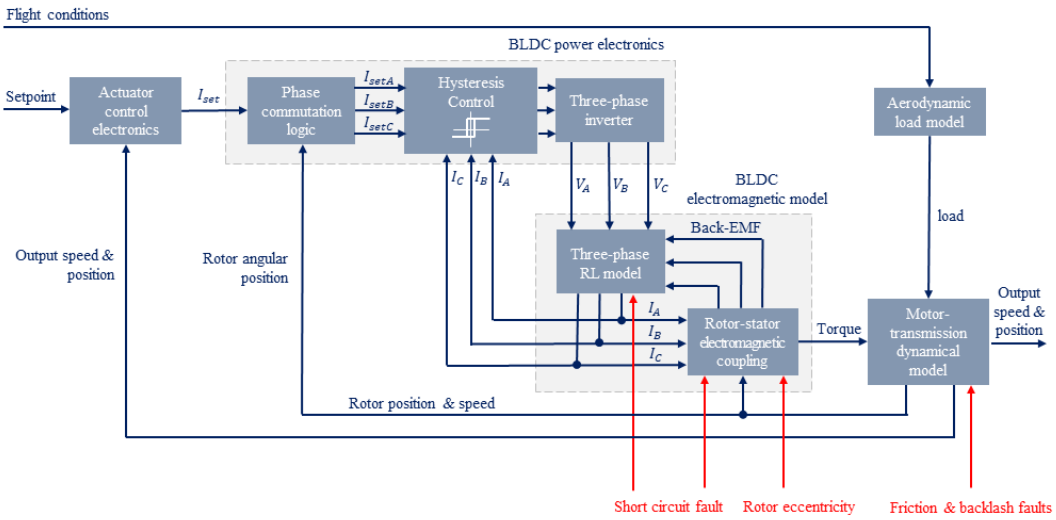

Fig. 2 Block diagram of the high-fidelity numerical model

The block diagram in Figure 2 illustrates the architecture of the high-fidelity EMA model. The actuator control electronics model emulates the Proportional Derivative Integrative (PID) control law, and defines the reference current I_r for the motor to neglect the error between the commanded setpoint of position and speed and the actual position and speed of the aerodynamic surface. This model accounts for signal noise and digitization, and the controller allows to switch between a position control mode and a speed control mode. The power electronics block models the three phase inverter providing a reliable estimate of the effects of the pulse width modulation three-phase current control logic, and defines the voltages V_A, V_B and V_C to produce the currents I_A, I_B and I_C required to achieve the torque setpoint. The electromagnetic model of the BrushLess Direct Current (BLDC) electric motor consists of a complete lumped parameters model of the electromagnetic coupling between the stator windings and the rotor poles to estimate the magnetic flux across the air gap. This block allows to compute the torque T_m produced by the motor, and accounts for multiple fault modes including the partial short circuit of the stator for the three phases (k_3, k_4 and k_5) and the rotor eccentricity (k_6 and k_7). The motor-transmission model is a nonlinear second order dynamical model of the motor and gearbox of the actuator, and determines the position of the aerodynamic surface θ_u and the position of the motor θ_m. This block is capable to consider nonlinear effects and faults that commonly affect the mechanical transmission, namely the dry friction between the components (k_1), and the transmission backlash (k_2). To simulate a real-word scenario, the high-fidelity model implements an aerodynamic load model block that provides a representation of the aerodynamic hinge moment acting on the actuator using the linearized longitudinal model of the F-16 fighter jet [55].

We consider this high-fidelity numerical model of the EMA as an emulator of a real-world actuator, and is adopted to assess the performance of FREEDOM in numerical experiments and to collect ground truth data in the offline compression stage. However, the computational cost required to estimate the dynamic of the EMA is almost two orders of magnitude above the simulated time interval, making the FDI task with the high-fidelity model unfeasible with

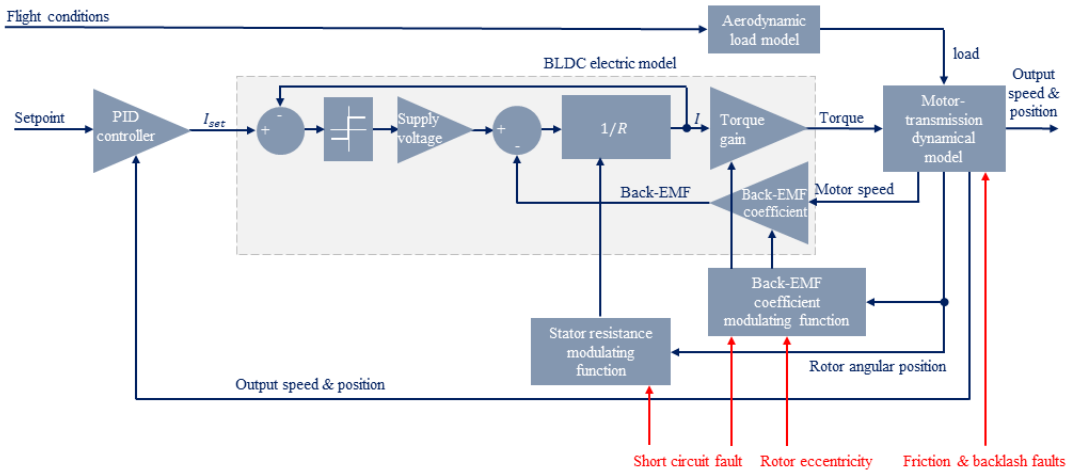

Fig. 3 Block diagram of the low-fidelity numerical model

limited computational resources. This motivates the development of a low-fidelity model of the EMA that introduces approximations to reduce the computational burden for evaluation while retaining an acceptable level of simulation accuracy.

2. Low-Fidelity Monitoring Model

The low-fidelity numerical model of the EMA system introduces simplifications in the physical modeling of the electrical subsystems of the actuator to contain the computational cost associated with its evaluation [52].

The architecture of the low-fidelity EMA model is illustrated in Figure 3. The main approximation introduced in this model is the three-phase inverter modeling and the evaluation of the magnetic flux across the air gap. Those complex and expensive to evaluate subsystems are replaced in the low-fidelity model with a first order direct current model assuming the inductance of the motor negligible. Accordingly, the simplified governing equation provides an approximated relation between the motor current I_m, voltage V_m and torque T_m as follows:

$$RI_m = V_m - \nu\omega \tag{18}$$

$$T_m = \nu I_m \tag{19}$$

where ν is the back-electromotive force coefficient, R is the resistance of the stator, and ω is the motor angular speed. To model the electrical failure modes of partial short circuit and rotor eccentricity $(k_3, \ldots, k_7)$, we follow the approach proposed by Berri et al. [56] modulating the electrical motor resistance, inductance and electromotive force coefficient as a function of the rotor angular position through two shape functions sensitive to faults: this strategy permits to

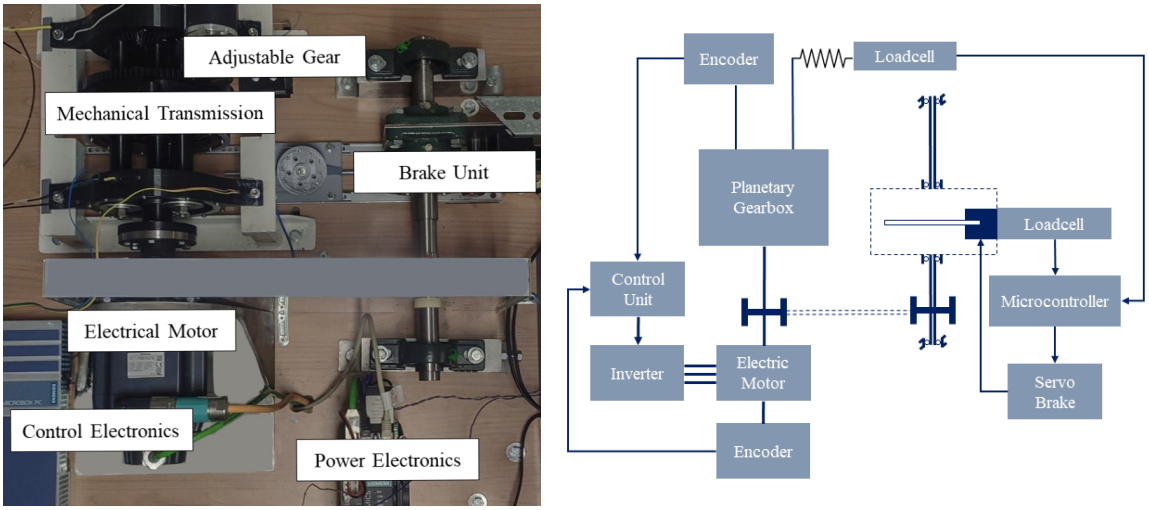

(a) **(b)**

Fig. 4 (a) EMA test-bench and (b) the corresponding block diagram

emulate the response of the high-fidelity model in presence of faults.

This modeling approach of the electrical power unit allows to avoid the iterative solution of the stator circuit, resulting in a reduced computational burden and acceptable numerical accuracy. In this paper, we use the low-fidelity model of the EMA to compute the monitoring current signal during the online FDI procedure.

B. Physical Test Bench of the System

The test bench of the EMA system provides experimental data about the dynamical behaviour of the system in different operating conditions and considering different fault modes [57]. In particular, the test bench allows to simulate the presence of mechanical faults affecting the system, namely the increase of the friction force k_1 and backlash k_2 in the mechanical transmission.

The layout of the EMA test-bench is illustrated in Figure 4. The electrical power unit consists of a permanent magnet synchronous motor characterized by a three-phase star connected permanent magnet architecture featuring four pole pairs. The power electronics coupled with the electrical motor consists of a driver powered by the $400V$ three-phase industrial line for the power module, and a $24V$ DC line for the logic subsystem. The control unit adopts an absolute encoder to measure the position of the motor shaft that is used to synchronize the phase commutation and to close the velocity control loop. The transmission subsystem is based on a planetary gearbox that converts the torque provided by the motor in a torque applied to the user shaft. The architecture of the transmission is conceived to introduce the backlash fault mode (k_2) through an adjustable gear that simulates the degradation of the mechanical components. The brake unit simulates the effects of external loads on the actuator connecting a disc brake to the motor shaft through a roller chain. Additionally, this subsystem emulates the transmission wear resulting in the increase of the friction force

(k_1) that is simulated increasing the load value applied to the motor shaft.

In this paper, the experimental data measured from the EMA test-bench are adopted to validate our Bayesian FDI strategy, providing the experimental reference current signal that is used to assess the health status of the system in presence of mechanical faults. Additionally, the test-bench data have been employed to validate the response of the high-fidelity numerical model of the EMA (Section III.A.1) in nominal conditions.

IV. Experiments

In the following, we demonstrate and validate our original methodology FREEDOM for the fault detection and isolation problem of the electromechanical actuator for aerospace applications discussed in Section III considering a variety of mechanical and electrical fault conditions.

For all the numerical experiments, we collect a reference dataset of 100 combinations of incipient faults whose corresponding system responses are evaluated with the high-fidelity EMA model (Section III.A.1). This set of faults is determined through a modified scaled Latin hypercube sampling to increase the density of sampling points near the nominal condition [19]. Offline, we use this dataset to compute an encoding map of $n_w = 30$ informative points using our original two-step compression strategy presented in Section II.A. Figure 5 shows the placement of those informative points determined through the self organizing map (Section II.A.2) for the first mode computed using the dynamic mode decomposition technique (Section II.A.1): our compression strategy places the n_w points in correspondence of the most significant locations of the mode including minima and maxima. This compressed representation is adopted online to identify the health status of the system through the inverse Bayesian fault detection and isolation algorithm illustrated in Section II.B. For this study, we use the Gaussian process (Section II.B.1) as the surrogate model implementing the square exponential kernel for the GP covariances, and the maximum likelihood technique to optimize the hyperparameters of the kernel and the mean function of the GP [58]. Additionally, we compare three formulations of the acquisition function (Section II.B.2), including the expected improvement (EI), upper-confidence bound (UCB) and two-step lookahead acquisition function (2lookEI).

We conducted both numerical and physical experiments considering three main experimental configurations to investigate the overall behaviour of the proposed methodology. In particular, we first tested FREEDOM implementing the high-fidelity numerical model of the EMA (Section III.A.1) to compute both the reference output signal and the monitoring signal: the goal is to assess the performance of the proposed methodology in the identification of the health status of the system without introducing a modeling error between the reference and the monitoring signals. This procedure permits to highlight the main difficulties in solving the EMA identification problem caused by the interaction of heterogeneous and multi-domain fault modes that affect simultaneously the system, and excludes the influence of modeling approximations in the computation of the monitoring signal. For the numerical test-cases, we compute the output signal considering in input a linear chirp command characterized by a 0.5 s duration, $5 \cdot 10^{-3}$ rad amplitude, 0

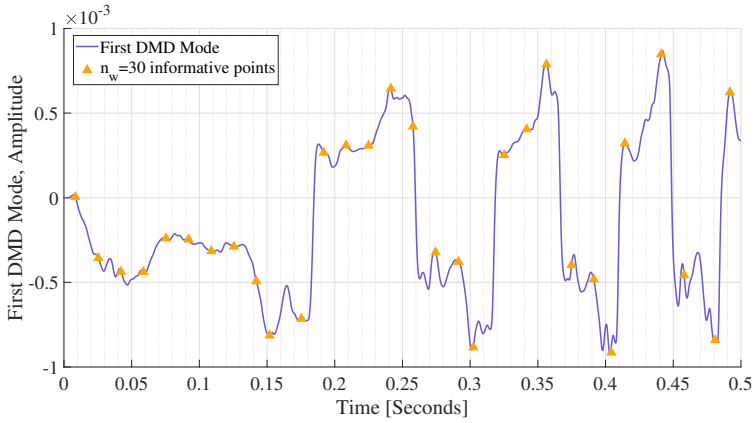

Fig. 5 Set of $n_w = 30$ informative points over the first DMD mode

Hz start frequency and 15 Hz end frequency, and an aerodynamic load of 0.5 Nm applied to the actuator.

Then, we investigate our methodology implementing the low-fidelity representation of the EMA (Section III.A.2) as the monitoring model, to evaluate the actual performance in fault identification considering a real-world scenario where a fast digital twin is required to limit the computational resources for the evaluation of the monitoring signal. This allows to assess both the accuracy and robustness of the proposed methodology in presence of multiple fault conditions and modeling error between reference and monitoring system.

Finally, we validate FREEDOM for the health assessment of the real-world EMA system (Section III.B) using the low-fidelity EMA model as the monitoring model. For the physical experiments, we provide in input to the test-bench and low-fidelity numerical model an input sinusoidal command with 0.12 rad amplitude and 0.2 Hz frequency, without external loads applied to the actuator.

The whole procedure is implemented in the Matlab environment, and we run all the experiments using a laptop PC equipped with Intel Core i7-6700HQ (2.6 GHz) and 32 GB of RAM.

V. Results and Discussion

In the following, we illustrate and discuss the results obtained with our original framework FREEDOM. To evaluate the performance of the algorithm, we define the following assessment metrics:

$$e(k_i) = \frac{||k_i^* - \widetilde{k}_i||}{k_i^*} \cdot 100 \tag{20}$$

$$\delta^* = \min(\delta(\boldsymbol{k}^*, \hat{\boldsymbol{x}})) \tag{21}$$

where k_i^* is the actual level of damage that affects the system, $\widetilde{k}_i$ is the level of damage inferred by the algorithm

considering the i-th fault mode, and $\delta(\boldsymbol{k}^*,\hat{\boldsymbol{x}})$ is the value of the discrepancy between the reference and monitoring output signals. In particular, $e(k_i)$ measures the percentage relative error in the identification of the health status of the system, and δ^* represents the minimum value of the discrepancy achieved by the algorithm.

We evaluate $e(k_i)$ and δ^* as functions of the time employed by the different algorithms to complete the FDI task. For the results obtained against numerical experiments, we consider a statistics over 100 different incipient faults combinations $\boldsymbol{k}^* = (k_1^*,...,k_7^*)$ including all the spectrum of mechanical and electrical damages. For the results obtained against physical experiments, we consider a statistics over 10 different combinations of incipient mechanical faults $\boldsymbol{k}^* = (k_1^*,k_2^*)$. For both the numerical and physical experiments, the incipient damage conditions are determined through the scaled Latin hypercube sampling proposed by Berri et al. [19]. This choice is motivated by the increased probability distribution of the fault combinations located near the nominal condition, in order to collect a large amount of incipient faults without limiting the identification process bounding the space of faults. In the remaining, the results are reported and discussed for all the three different formulations of our FDI algorithm – namely Expected Improvement (EI), Upper-Confidence Bound (UCB), Two-Step Lookahead Expected Improvement (2lookEI) – and compared in term of median values of the inference error $e(k_i)$ and discrepancy δ^* together with the associated statistics in between the 25-th and 75-th percentiles.

Numerical Experiments: High-Fidelity Monitoring

Figure 6 shows the outcomes obtained for an experimental setup where the high-fidelity numerical model of the EMA (Section III.A.1) is used as the source of information for both the reference and monitoring current signal. All the competing formulations identify the current health status of the system reducing the inference error $e(k_i)$ for both the mechanical (k_1,k_2) and electrical faults (k_3,k_4,k_5,k_6,k_7). The best performing FDI strategy implements the two-step lookahead acquisition function (2lookEI). which leads to a significant reduction of the inference error for all the fault modes with a fraction of the computational time required by UCB and EI. This outcome suggests that acquisition functions capable to quantify the improvement in the solution of the FDI problem achievable in future iterations determine an effective and efficient sampling scheme to identify the health status of the system.

It should be noticed that the correct identification of the health status of the EMA – which correspond to the computational time for which the inference error is equal to zero – coincides with null discrepancy between the reference and monitoring current signals (Figure 6h). These results are justified from the adoption of the same high-fidelity numerical model to compute both the reference and monitoring signals. As a consequence, the inference of the actual damage configuration affecting the EMA produces the same reference and monitoring responses, which in turn determine a value of the discrepancy function equal to zero. This experimental setting offers the opportunity to investigate the challenges associated with the EMA health assessment problem without a modeling error between the diagnostics signals that might lead to the misinterpretation of the results. In particular, the overall outcomes achieved

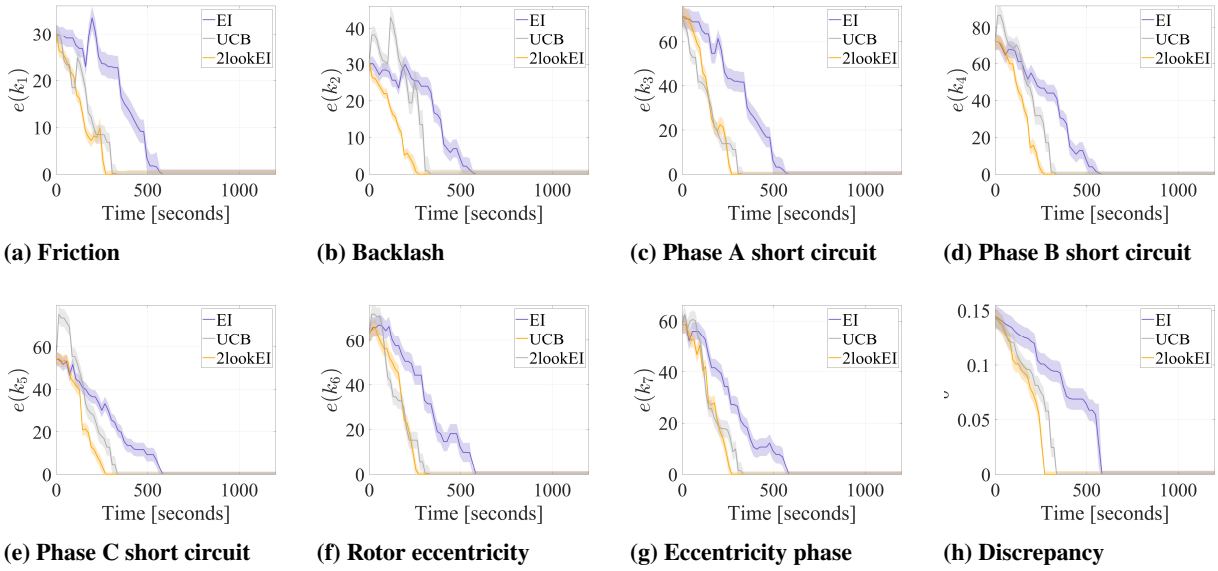

Fig. 6 Statistics over 100 incipient fault conditions of the percentage relative error of the inference of the fault parameters $e(k_i)$ and minimum discrepancy value δ^* obtained for the high-fidelity monitoring.

with the three formulations for all the fault modes indicate that a reduction of the discrepancy between the reference and monitoring current signal is not related with a continuous decrease of the inference error (Figure 6). This suggests that the EMA identification problem is ill-posed: a reduction of the discrepancy function is not always related to an improvement in the accuracy of the faults inference. As a consequence, the identified fault parameters are subjected to instability and uncertainty that raise when the reduction of the discrepancy causes an increase in the inference error, further complicating the fault detection and isolation task. These results are justified with the presence of multiple and multiphysics faults affecting simultaneously the EMA system. In particular, a variation of both the friction in the mechanical transmission (k_1) and the partial short circuit in the three phases of the electric motor (k_3, k_4, k_5) determines opposite effects in the dynamical response of the system: increasing k_1 reduces the speed of the actuation while increasing $k_{3:5}$ causes an increase in the motor speed. These effects indicate a distinct multimodality of the discrepancy function, which is characterized by the presence of multiple suboptimal local minima that stresses the search towards the actual health status of the system. The outcomes show that FREEDOM is capable to address this multimodal behaviour through the joint contribution of the efficient compression stage and the Bayesian scheme: the two-step compression extracts the most significant elements of the signals that are used to guide and support with an highly informative content the Bayesian scheme for inference; this produces an effective FDI procedure with contained evaluations of the monitoring model of the system.

Table 2 and Table 3 summarize the convergence results for the three formulations of the acquisition function in terms of median values of the inference error $e(k_i)$ and minimum discrepancy δ^*, and maximum inference error $e_{max}(k_i)$ achieved at convergence, respectively. In particular, the computational time required to identify the exact health status

Method	$e(k_1)$	$e(k_2)$	$e(k_3)$	$e(k_4)$	$e(k_5)$	$e(k_6)$	$e(k_7)$	δ^*	Time
EI	0.00%	0.00%	0.00%	0.00%	0.00%	0.00%	0.00%	0.00	583 s
UCB	0.00%	0.00%	0.00%	0.00%	0.00%	0.00%	0.00%	0.00	335 s
2lookEI	0.00%	0.00%	0.00%	0.00%	0.00%	0.00%	0.00%	0.00	271 s

Table 2 Convergence results of the percentage relative error of the inference of the fault parameters $e(k_i)$, minimum discrepancy value δ^*, and computational time obtained for the high-fidelity monitoring.

Method	$e_{max}(k_1)$	$e_{max}(k_2)$	$e_{max}(k_3)$	$e_{max}(k_4)$	$e_{max}(k_5)$	$e_{max}(k_6)$	$e_{max}(k_7)$
EI	1.06%	1.05%	1.53%	1.51%	1.07%	1.43%	1.16%
UCB	0.87%	1.30%	1.10%	1.64%	1.35%	1.26%	1.13%
2lookEI	0.88%	0.91%	1.21%	1.25%	0.95%	1.20%	1.05%

Table 3 Convergence results of the maximum percentage relative error of the inference of the fault parameters $e_{max}(k_i)$ obtained for the high-fidelity monitoring.

of the EMA system is on average 271 seconds for the 2lookEI, while the other competing formulations require further time expenditure to infer the damaged condition (Table 2). A significant outcome observed at convergence is that all the algorithms achieve a maximum inference error lower than 1.64% over the experimental setup of 100 incipient fault combinations, highlighting the robust identification of the health status of the system (Table 3).

The results obtained for the high-fidelity monitoring test-case demonstrate the accuracy and robustness of the framework FREEDOM in presence of multiple and interacting incipient failure modes. In addition, it is shown the capability of our framework to overcome the issues related to the ill-posed identification problem and multimodality of the discrepancy function. However, the demand for computational resources makes the FDI procedure with high-fidelity numerical models unfeasible for the fast identification of the health status of the system. This justifies the adoption of the low-fidelity numerical model to approximate the output signal of the system, decreasing the computational cost required for the FDI procedure.

Numerical Experiments: Low-Fidelity Monitoring

Figure 7 illustrates the outcomes achieved adopting the low-fidelity numerical model of the EMA system (Section III.A.2) to compute the monitoring current signal. The 2lookEI acquisition function leads to a superior reduction of the inference error with a contained computational time if compared with EI and UCB. Nevertheless, all the competing formulations identify accurately the level of damage for the electrical faults (k_3, k_4, k_5, k_6, k_7) and allow to reduce the inference error for friction (k_1) and backlash (k_2) fault modes below the 6.66% and 10.1%, respectively. However, the convergence values of $e(k_1)$ and $e(k_2)$ are higher with respect to the values of the error for the electrical faults. Figure 7a and Figure 7b report the convergence history of the inference error for the mechanical faults affecting the EMA. Both $e(k_1)$ and $e(k_2)$ show similar trends: the error decreases for lower computational times while tends to reach values

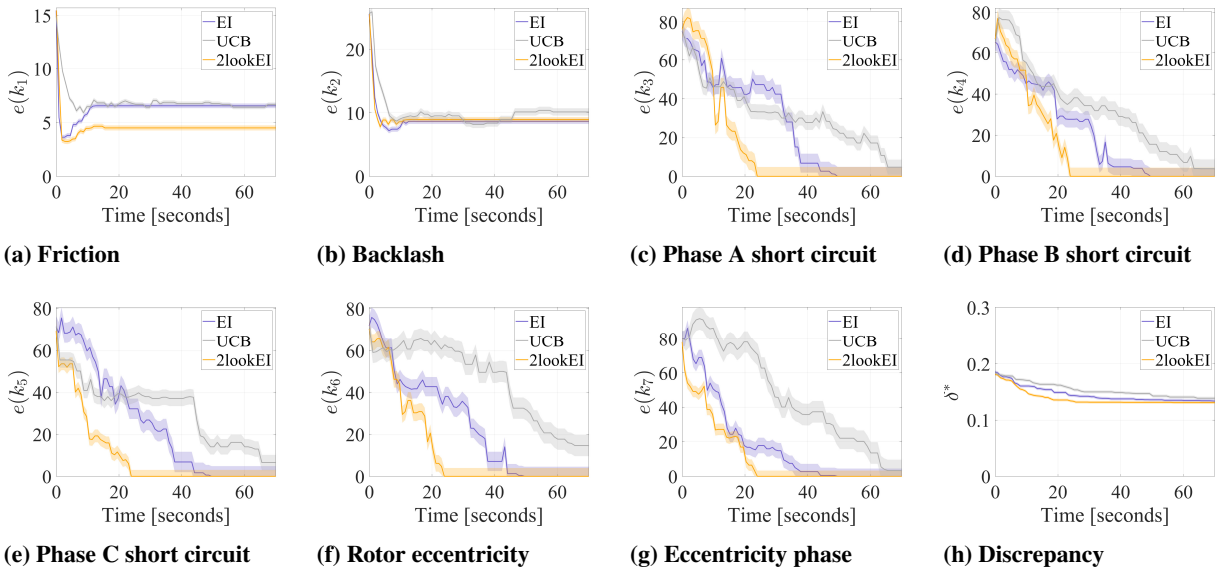

(a) Friction **(b) Backlash** **(c) Phase A short circuit** **(d) Phase B short circuit**

(e) Phase C short circuit **(f) Rotor eccentricity** **(g) Eccentricity phase** **(h) Discrepancy**

Fig. 7 Statistics over 100 incipient fault conditions of the percentage relative error of the inference of the fault parameters $e(k_i)$ and minimum discrepancy value δ^* obtained for the low-fidelity monitoring.

higher than the minimum computed so far as the FDI algorithm proceeds in reducing the discrepancy δ. This result can be justified with the introduction of a modeling error between the reference – high-fidelity – and monitoring – low-fidelity – signals that is reflected in a computed minimum of the discrepancy δ^* different from zero (Figure 7h). Indeed, the same combination of fault parameters determines discrepant current responses between the high-fidelity and low-fidelity numerical model caused by the physical approximations adopted to reduce the computational cost of the low-fidelity representation. Those effects poses further difficulties to efficiently assess the health status of the system.

Table 4 illustrates the median values of the inference error $e(k_i)$ and minimium discrepancy δ^* reached at the convergence of the FDI process, while Table 5 shows the corresponding maximum inference error $e_{max}(k_i)$. In particular, the 2lookEI infers the electrical faults with an error below the 0.12%, while permits the identification of the mechanical faults with an error of the 4.51% and 8.94% for friction and backlash, respectively (Table 4). Although the inference of mechanical failures is not as accurate as the identification of electrical damages, the overall accuracy of our methodology is adequate for the detection of incipient failure modes, and permits the adoption of corrective actions to contain the early stage effects on the degradation of the system performance. In addition, the identification of the health status of the system requires on average 25 seconds for the 2lookEI, which correspond to a reduction of the 91% if compared with the time required to assess the EMA health status with the high-fidelity monitoring. This allows to infer barely noticeable failure modes early on before the propagation, and permits to prevent and counteract to excessive loss of performance of the system with potentially severe effects.

Moreover, it can be noticed that the 2lookEI algorithm achieves a maximum inference error at convergence below the 4.81% for the electrical damages, and equal to 4.73% for friction and 9.33% for backlash considering a total of 100

Method	$e(k_1)$	$e(k_2)$	$e(k_3)$	$e(k_4)$	$e(k_5)$	$e(k_6)$	$e(k_7)$	δ^*	Time
EI	6.55%	8.66%	0.08%	0.09%	0.11%	0.10%	0.05%	0.136	51 s
UCB	6.66%	10.1%	4.73%	3.68%	6.50%	14.7%	3.35%	0.139	69 s
2lookEI	4.51%	8.94%	0.05%	0.09%	0.12%	0.07%	0.06%	0.132	25 s

Table 4 Convergence results of the percentage relative error of the inference of the fault parameters $e(k_i)$, minimum discrepancy value δ^*, and computational time obtained for the low-fidelity monitoring.

Method	$e_{max}(k_1)$	$e_{max}(k_2)$	$e_{max}(k_3)$	$e_{max}(k_4)$	$e_{max}(k_5)$	$e_{max}(k_6)$	$e_{max}(k_7)$
EI	6.77%	9.07%	4.90%	4.05%	4.82%	4.61%	4.53%
UCB	6.86%	10.73%	8.60%	8.21%	10.23%	19.77%	9.64%
2lookEI	4.73%	9.33%	4.81%	4.24%	3.12%	3.98%	3.35%

Table 5 Convergence results of the maximum percentage relative error of the inference of the fault parameters $e_{max}(k_i)$ obtained for the low-fidelity monitoring.

Metric	GA	PSO	DE	GWO	FREEDOM
Average Time	2322 s	1710 s	405 s	709 s	25 s
Average Error $e(\boldsymbol{k})$	2.813%	0.711%	3.001%	4.378%	1.977%

Table 6 Comparison of the computational time and average inference error between the FREEDOM algorithm and the meta-heuristic algorithms proposed by [59], namely Genetic Algorithm (GA), Particle Swarm Optimization (PSO), Differential Evolution (DE) and Grey Wolf Optimization (GWO).

incipient fault combinations (Table 5). These outcomes demonstrate that our methodology FREEDOM provides a robust identification of the health status of the system even in presence of modeling errors, ill-posedness, and multimodality of the identification problem. However, the maximum inference error computed at convergence is higher if compared with the outcomes of the high-fidelity monitoring test-case (Table 3), suggesting that the introduction of the modeling error also affects the overall robustness of the FDI process.

Table 6 compares the results obtained with the FREEDOM algorithm and with popular meta-heuristic approaches as the one proposed by Dalla Vedova et al. [59]. In particular, we compare the two-step lookahead implementation of FREEDOM with the diagnostics outcomes obtained with Genetic Algorithm (GA), Particle Swarm Optimization (PSO), Differential Evolution (DE) and Grey Wolf Optimization (GWO). FREEDOM is capable to achieve a comparable average reduction of the inference error with a remarkable acceleration up to two orders of magnitude if compared with the standard algorithms. These results remark and emphasize the capability of the FREEDOM framework to leverage the combination of efficiently compressed highly informative signals with the Bayesian inference stage to provide an accurate health status assessment with a fraction of the computational cost required by competing algorithms.

The outcomes computed adopting the low-fidelity numerical model demonstrate a substantial acceleration of the inference of incipient damages with satisfactory accuracy and robustness. In particular, the implementation of a

low-fidelity monitoring model significantly reduces the computational burden associated with the FDI procedure if compared with the time expenditure required for the high-fidelity monitoring test-case. Moreover, the computational time required to complete the FDI task with our methodology is two orders of magnitude lower than state of the art model-based FDI algorithms [3, 9, 59, 60]. This reveals the capabilities of our algorithm to efficiently exploit data from the low-fidelity monitoring model and contain the demand for computing resources. However, the introduction of a modeling error between the reference and monitoring signal moderately affects the accuracy and robustness of the FDI procedure for the failures in the mechanical transmission.

Real-World Experiments

Figure 8 illustrates the results obtained with the FREEDOM algorithm for the health assessment of the real-world EMA system (Section III.B) implementing the low-fidelity monitoring model. All the three formulations are capable to identify the health status of the system minimizing the inference error with a contained computational time. The overall convergence trends for both the inference error of friction (Figure 8a) and backlash (Figure 8b) confirm that the identification problem is ill-posed and multimodal – the decrease of the discrepancy (Figure 8c) is not always related to a reduction of the inference error – and affected by the modeling error between the current signal measured on the real-world system and the same signal computed with the low-fidelity model – the minimum of the discrepancy is greater than zero when the health status of the system is inferred.

Table 7 provides the experimental convergence median values of the inference error $e(k_i)$ and minimum discrepancy δ^* for the three acquisition functions considered in this paper. All the implementations accurately identify the health status of the system, and lead to an inference error of the 0.03% for friction and 0.08% for backlash. However, the 2lookEI implementation achieves the best experimental results in terms of efficiency, identifying the incipient mechanical faults with a computational time within 6 seconds; this corresponds to a reduction of the 62% and 70% of time expenditure if compared with the outcomes of the EI and UCB methods, respectively. Table 8 illustrates the maximum inference errors $e_{max}(k_i)$ at convergence. All the formulations keep the maximum error below the 3.35%, validating the robust identification of the incipient mechanical faults; in particular, the two-step lookahead acquisition function shows the higher level of robustness with an inference error at convergence lower than the 1.62% and 1.24% for friction and backlash, respectively.

These outcomes validate the performance of FREEDOM as a computational framework that enables the acceleration of the FDI procedure, and permits the accurate and robust identification of incipient faults affecting a complex and multiphysics aerospace system. A significant achievement of our methodology is the reduction of computational time required to identify the health status of the real-system, which corresponds to an inference procedure two orders of magnitude faster than standard model-based FDI approaches [3, 9, 59, 60].

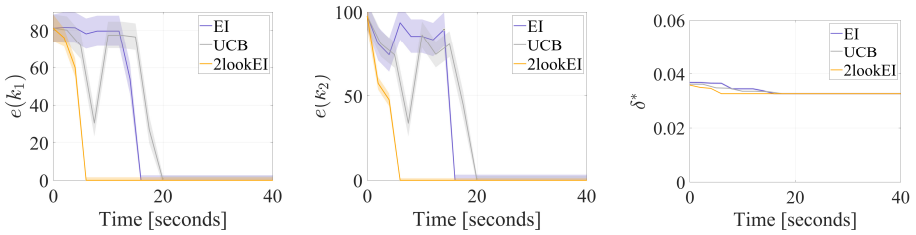

(a) Friction **(b) Backlash** **(c) Discrepancy**

Fig. 8 Statistics over 10 incipient fault conditions of the percentage relative error of the inference of the fault parameters $e(k_i)$ and minimum discrepancy value δ^* obtained for the real-world experiments.

Method	$e(k_1)$	$e(k_2)$	δ^*	Time
EI	0.03%	0.08%	0.0326	16 s
UCB	0.03%	0.08%	0.0326	20 s
2lookEI	0.03%	0.08%	0.0326	6 s

Table 7 Convergence results of the percentage relative error of the inference of the fault parameters $e(k_i)$, minimum discrepancy value δ^*, and computational time obtained for the real-world experiments.

Method	$e_{max}(k_1)$	$e_{max}(k_2)$
EI	2.69%	3.35%
UCB	2.39%	2.59%
2lookEI	1.62%	1.24%

Table 8 Convergence results of the maximum percentage relative error of the inference of the fault parameters $e_{max}(k_i)$ obtained for the real-world experiments.

VI. Concluding Remarks

This paper introduces an original fault detection and isolation (FDI) methodology FREEDOM to accelerate the identification of the health status of complex aerospace systems. Our algorithm permits to identify the incipient failure condition affecting the system through the original combination of a two-step compression strategy – which reduces the amount of data to be stored and processed – and an inverse Bayesian approach – to infer failure modes through the efficient use of data. The objective is to accelerate the FDI task and provide an accurate and robust inference of the system health status with a major reduction of the demand for computational resources. In addition, the use of the Bayesian framework opens the avenue to formalize the reliability of the prediction based on the stochastic nature of the Gaussian process surrogate model.

Without losing the general applicability of our method, we demonstrate and validate our computational framework for the fault detection and isolation problem of an electromechanical actuator, considering heterogeneous mechanical and electrical incipient fault modes. Specifically, we conducted both numerical and physical experiments comparing three formulations of the Bayesian acquisition function to investigate the performance of our methodology with different

search criteria. The results demonstrate that FREEDOM provides an accurate and robust inference of the health status of the system in presence of incipient faults with a reduced time expenditure. This is particularly relevant to capture the early stages of damages propagation, and prevents severe effects due to the degradation of the performance of the system.

The comparison over the different formulations reveals that the two-step lookahead acquisition function provides a robust identification of the electrical faults with an error below the 0.1% while keeping the error under the 9% for the mechanical damages; this is due to the intrinsic properties of the low-fidelity monitoring model that introduces a modeling error which increases the difficulties in the identification of mechanical faults. Nevertheless, the major outcome is observed in terms of a large reduction of the computational time required to complete the FDI task. Indeed, the fault detection and isolation procedure is completed within 25 seconds when the low-fidelity monitoring model is used implementing the two-step lookahead acquisition function. This corresponds to a reduction of two orders of magnitude with respect to the computational cost required by standard model-based FDI algorithms. The outcomes are validated through physical experiments on the real-world system affected by mechanical failures. In particular, the two-step lookahead acquisition function permits to achieve the exact identification of the health status of the system within 6 seconds with the use of the low-fidelity monitoring model.

The major acceleration of the FDI procedure is enabled by the original combination of a highly informative two-step compression mapping that allows to speed up the data processing, and the data efficient Bayesian inference that permits to contain the number of model evaluations. As an additional remarkable outcome, we achieve sensitive improvements in terms of computational effort while enabling an accurate identification of incipient multimodal damages. We recognize that this potentially paves the way for a major acceleration of the adoption of novel technologies onboard, whose integration and associated increase in system complexity requires an efficient FDI procedure suitable for onboard health monitoring. This would ideally speed up the achievement of the ambitious goals of sustainable aviation, towards net-zero climate impact.

Our experiments illustrate that the adoption of a low-fidelity monitoring model – and therefore the introduction of a modeling error between the reference and monitoring signals – affects the fault detection and isolation process, precluding the possibility of high accuracy in health status inference. We believe that approaches to overcome this issue are offered by multifidelity methods which we plan to consider in future developments.

Acknowledgments

This work was supported by project Multisource Frameworks to Support Real-time Structural Assessment and Autonomous Decision Making under the Visiting Professor program of Politecnico di Torino, and by the University's Doctoral Scholarship. Additional acknowledgement to Prof. Paolo Maggiore for the support.

References

[1] Upham, P., Maughan, J., Raper, D., and Thomas, C., *Towards sustainable aviation*, Routledge, 2012.

[2] Ranasinghe, K., Sabatini, R., Gardi, A., Bijjahalli, S., Kapoor, R., Fahey, T., and Thangavel, K., "Advances in Integrated System Health Management for mission-essential and safety-critical aerospace applications," *Progress in Aerospace Sciences*, Vol. 128, 2022, p. 100758. https://doi.org/https://doi.org/10.1016/j.paerosci.2021.100758.

[3] Yin, Z., Hu, N., Chen, J., Yang, Y., and Shen, G., "A review of fault diagnosis, prognosis and health management for aircraft electromechanical actuators," *IET Electric Power Applications*, Vol. 16, No. 11, 2022, pp. 1249–1272. https://doi.org/https://doi.org/10.1049/elp2.12225.

[4] Mansouri, M., Harkat, M.-F., Nounou, H., and Nounou, M. N., *Data-driven and model-based methods for fault detection and diagnosis*, Elsevier, 2020. https://doi.org/https://doi.org/10.1016/c2018-0-04213-9.

[5] Cen, J., Yang, Z., Liu, X., Xiong, J., and Chen, H., "A review of data-driven machinery fault diagnosis using machine learning algorithms," *Journal of Vibration Engineering & Technologies*, 2022, pp. 1–27. https://doi.org/https://doi.org/10.1007/s42417-022-00498-9.

[6] Freeman, P., Pandita, R., Srivastava, N., and Balas, G. J., "Model-based and data-driven fault detection performance for a small UAV," *IEEE/ASME Transactions on mechatronics*, Vol. 18, No. 4, 2013, pp. 1300–1309. https://doi.org/https://doi.org/10.1109/tmech.2013.2258678.

[7] Tinga, T., and Loendersloot, R., "Physical model-based prognostics and health monitoring to enable predictive maintenance," *Predictive Maintenance in Dynamic Systems*, Springer, 2019, pp. 313–353. https://doi.org/https://doi.org/10.1007/978-3-030-05645-2_11.

[8] Engelberth, T., Krawczyk, D., and Verl, A., "Model-based method for condition monitoring and diagnosis of compressors," *Procedia Cirp*, Vol. 72, 2018, pp. 1321–1326. https://doi.org/https://doi.org/10.1016/j.procir.2018.03.271.

[9] Dalla Vedova, M. D. L., Germanà, A., Berri, P. C., and Maggiore, P., "Model-based fault detection and identification for prognostics of electromechanical actuators using genetic algorithms," *Aerospace*, Vol. 6, No. 9, 2019, p. 94. https://doi.org/https://doi.org/10.3390/aerospace6090094.

[10] Kolcio, K. O., "Model-based fault detection and isolation system for increased autonomy," *AIAA SPACE 2016*, American Institute of Aeronautics and Astronautics, 2016, p. 5225. https://doi.org/https://doi.org/10.2514/6.2016-5225.

[11] Venkataraman, R., and Seiler, P. J., "Model-based detection and isolation of rudder faults for a small UAS," *AIAA Guidance, Navigation, and Control Conference*, 2015, p. 0857. https://doi.org/https://doi.org/10.2514/6.2015-0857.

[12] Sidhu, A., Izadian, A., and Anwar, S., "Adaptive nonlinear model-based fault diagnosis of Li-ion batteries," *IEEE Transactions on Industrial Electronics*, Vol. 62, No. 2, 2014, pp. 1002–1011. https://doi.org/https://doi.org/10.1109/tie.2014.2336599.

[13] Garcia Garriga, A., Ponnusamy, S. S., and Mainini, L., "A multi-fidelity framework to support the design of More-Electric Actuation," *AIAA AVIATION 2018 Multidisciplinary Analysis and Optimization Conference*, 2018, p. 3741. https://doi.org/https://doi.org/10.2514/6.2018-3741.

[14] Garriga, A. G., Mainini, L., and Ponnusamy, S. S., "A machine learning enabled multi-fidelity platform for the integrated design of aircraft systems," *Journal of Mechanical Design*, Vol. 141, No. 12, 2019. https://doi.org/https://doi.org/10.1115/1.4044401.

[15] Schäfer, A. W., Barrett, S. R., Doyme, K., Dray, L. M., Gnadt, A. R., Self, R., O'Sullivan, A., Synodinos, A. P., and Torija, A. J., "Technological, economic and environmental prospects of all-electric aircraft," *Nature Energy*, Vol. 4, No. 2, 2019, pp. 160–166. https://doi.org/https://doi.org/10.1038/s41560-018-0294-x.

[16] Wheeler, P., "Technology for the more and all electric aircraft of the future," *2016 IEEE International Conference on Automatica (ICA-ACCA)*, IEEE, 2016, pp. 1–5. https://doi.org/https://doi.org/10.1109/ica-acca.2016.7778519.

[17] Barzkar, A., and Ghassemi, M., "Electric power systems in more and all electric aircraft: A review," *Ieee Access*, Vol. 8, 2020, pp. 169314–169332. https://doi.org/https://doi.org/10.1109/access.2020.3024168.

[18] Sarlioglu, B., and Morris, C. T., "More electric aircraft: Review, challenges, and opportunities for commercial transport aircraft," *IEEE transactions on Transportation Electrification*, Vol. 1, No. 1, 2015, pp. 54–64. https://doi.org/https://doi.org/10.1109/tte.2015.2426499.

[19] Berri, P. C., Dalla Vedova, M. D. L., and Mainini, L., "Real-time fault detection and prognostics for aircraft actuation systems," *AIAA Scitech 2019 Forum*, 2019, p. 2210. https://doi.org/https://doi.org/10.2514/6.2019-2210.

[20] Mainini, L., "Structural assessment and sensor placement strategy for self-aware aerospace vehicles," *Structural Health Monitoring 2017*, 2017. https://doi.org/https://doi.org/10.12783/shm2017/14035.

[21] Mainini, L., and Willcox, K. E., "Sensor placement strategy to inform decisions," *18th AIAA/ISSMO Multidisciplinary Analysis and Optimization Conference*, 2017, p. 3820. https://doi.org/https://doi.org/10.2514/6.2017-3820.

[22] Schmid, P. J., "Dynamic mode decomposition of numerical and experimental data," *Journal of fluid mechanics*, Vol. 656, 2010, pp. 5–28. https://doi.org/https://doi.org/10.1017/s0022112010001217.

[23] Schmid, P. J., Li, L., Juniper, M. P., and Pust, O., "Applications of the dynamic mode decomposition," *Theoretical and Computational Fluid Dynamics*, Vol. 25, No. 1, 2011, pp. 249–259. https://doi.org/https://doi.org/10.1007/s00162-010-0203-9.

[24] Zhao, M., Zhao, Y., and Liu, Z., "Dynamic mode decomposition analysis of flow characteristics of an airfoil with leading edge protuberances," *Aerospace Science and Technology*, Vol. 98, 2020, p. 105684. https://doi.org/https://doi.org/10.1016/j.ast.2020.105684.

[25] Cartocci, N., Monarca, A., Costante, G., Fravolini, M. L., Dogan, K. M., and Yucelen, T., "Linear Control of a Nonlinear Aerospace System via Extended Dynamic Mode Decomposition," *AIAA Scitech 2022 Forum*, 2022, p. 2046. https://doi.org/https://doi.org/10.2514/6.2022-2046.vid.

[26] Deem, E. A., Cattafesta, L. N., Hemati, M. S., Zhang, H., Rowley, C., and Mittal, R., "Adaptive separation control of a laminar boundary layer using online dynamic mode decomposition," *Journal of Fluid Mechanics*, Vol. 903, 2020. https://doi.org/https://doi.org/10.1017/jfm.2020.546.

[27] Wall, M. E., Rechtsteiner, A., and Rocha, L. M., "Singular value decomposition and principal component analysis," *A practical approach to microarray data analysis*, Springer, 2003, pp. 91–109. https://doi.org/https://doi.org/10.1007/0-306-47815-3_5.

[28] Kohonen, T., "The self-organizing map," *Proceedings of the IEEE*, Vol. 78, No. 9, 1990, pp. 1464–1480. https://doi.org/10.1109/5.58325.

[29] Kohonen, T., *Self-organizing maps*, Vol. 30, Springer Science & Business Media, 2012. https://doi.org/https://doi.org/10.1007/978-3-642-56927-2.

[30] Baptista, M. L., Henriques, E. M., and Goebel, K., "A self-organizing map and a normalizing multi-layer perceptron approach to baselining in prognostics under dynamic regimes," *Neurocomputing*, Vol. 456, 2021, pp. 268–287. https://doi.org/https://doi.org/10.1016/j.neucom.2021.05.031.

[31] Rigamonti, M., Baraldi, P., Alessi, A., Zio, E., Astigarraga, D., and Galarza, A., "An ensemble of component-based and population-based self-organizing maps for the identification of the degradation state of insulated-gate bipolar transistors," *IEEE Transactions on Reliability*, Vol. 67, No. 3, 2018, pp. 1304–1313. https://doi.org/https://doi.org/10.1109/tr.2018.2834828.

[32] Jin, X., Que, Z., Sun, Y., Guo, Y., and Qiao, W., "A data-driven approach for bearing fault prognostics," *IEEE Transactions on Industry Applications*, Vol. 55, No. 4, 2019, pp. 3394–3401. https://doi.org/https://doi.org/10.1109/ias.2018.8544586.

[33] Oja, E., "Simplified neuron model as a principal component analyzer," *Journal of mathematical biology*, Vol. 15, No. 3, 1982, pp. 267–273. https://doi.org/https://doi.org/10.1007/bf00275687.

[34] Mockus, J., Tiesis, V., and Zilinskas, A., "The application of Bayesian methods for seeking the extremum," *Towards global optimization*, Vol. 2, No. 117-129, 1978, p. 2.

[35] Snoek, J., Larochelle, H., and Adams, R. P., "Practical bayesian optimization of machine learning algorithms," *Advances in neural information processing systems*, Vol. 25, 2012.

[36] Frazier, P. I., "A tutorial on Bayesian optimization," *arXiv preprint arXiv:1807.02811*, 2018.

[37] Bui-Thanh, T., "The Optimality of Bayes' Theorem," *SIAM news*, Vol. 54, No. 6, 2021.

[38] Jim, T. M., Faza, G. A., Palar, P. S., and Shimoyama, K., "Bayesian optimization of a low-boom supersonic wing planform," *AIAA journal*, Vol. 59, No. 11, 2021, pp. 4514–4529. https://doi.org/https://doi.org/10.2514/1.j060225.

[39] Yamaguchi, K., Phenisee, S. E., Chen, Z., Salviato, M., and Yang, J., "Ply-drop design of non-conventional laminated composites using Bayesian optimization," *Composites Part A: Applied Science and Manufacturing*, Vol. 139, 2020, p. 106136. https://doi.org/https://doi.org/10.1016/j.compositesa.2020.106136.

[40] Saves, P., Bartoli, N., Diouane, Y., Lefebvre, T., Morlier, J., David, C., Van, E. N., and Defoort, S., "Constrained Bayesian optimization over mixed categorical variables, with application to aircraft design," *Proceedings of the International Conference on Multidisciplinary Design Optimization of Aerospace Systems (AEROBEST 2021)*, 2021, pp. 1–758.

[41] Brevault, L., Balesdent, M., and Hebbal, A., "Multi-objective multidisciplinary design optimization approach for partially reusable launch vehicle design," *Journal of Spacecraft and Rockets*, Vol. 57, No. 2, 2020, pp. 373–390. https://doi.org/https://doi.org/10.2514/1.a34601.

[42] Rasmussen, C. E., "Gaussian processes in machine learning," *Summer school on machine learning*, Springer, 2003, pp. 63–71.

[43] Schulz, E., Speekenbrink, M., and Krause, A., "A tutorial on Gaussian process regression: Modelling, exploring, and exploiting functions," *Journal of Mathematical Psychology*, Vol. 85, 2018, pp. 1–16. https://doi.org/https://doi.org/10.1101/095190.

[44] Wahba, G., *Spline models for observational data*, SIAM, 1990. https://doi.org/https://doi.org/10.1137/1.9781611970128.

[45] Berkenkamp, F., Krause, A., and Schoellig, A. P., "Bayesian optimization with safety constraints: safe and automatic parameter tuning in robotics," *Machine Learning*, 2021, pp. 1–35. https://doi.org/https://doi.org/10.1007/s10994-021-06019-1.

[46] Jones, D. R., Schonlau, M., and Welch, W. J., "Efficient global optimization of expensive black-box functions," *Journal of Global optimization*, Vol. 13, No. 4, 1998, pp. 455–492. https://doi.org/https://doi.org/10.1023/A:1008306431147.

[47] Srinivas, N., Krause, A., Kakade, S. M., and Seeger, M., "Gaussian process optimization in the bandit setting: No regret and experimental design," *International Conference on Machine Learning*, PMLR, 2010, pp. 1015—1022.

[48] Wu, J., and Frazier, P., "Practical two-step lookahead Bayesian optimization," *Advances in neural information processing systems*, Vol. 32, 2019, pp. 9813–9823.

[49] Wilson, J. T., Hutter, F., and Deisenroth, M. P., "Maximizing acquisition functions for Bayesian optimization," *arXiv preprint arXiv:1805.10196*, 2018.

[50] Balaban, E., Bansal, P., Stoelting, P., Saxena, A., Goebel, K. F., and Curran, S., "A diagnostic approach for electro-mechanical actuators in aerospace systems," *2009 IEEE Aerospace conference*, IEEE, 2009, pp. 1–13. https://doi.org/https://doi.org/10.1109/aero.2009.4839661.

[51] Balaban, E., Saxena, A., Narasimhan, S., Roychoudhury, I., Goebel, K. F., and Koopmans, M. T., "Airborne electro-mechanical actuator test stand for development of prognostic health management systems," Tech. rep., NATIONAL AERONAUTICS AND SPACE ADMINISTRATION MOFFETT FIELD CA AMES RESEARCH . . . , 2010.

[52] Berri, P. C., Dalla Vedova, M. D. L., and Mainini, L., "Learning for predictions: Real-time reliability assessment of aerospace systems," *AIAA Journal*, Vol. 60, No. 2, 2022, pp. 566–577. https://doi.org/https://doi.org/10.2514/1.j060664.

[53] Belmonte, D., Dalla Vedova, M. D., and Maggiore, P., "Prognostics of Onboard Electromechanical Actuators: A New Approach Based on Spectral Analysis Techniques," *International Review of Aerospace Engineering*, Vol. 11, No. 3, 2018, pp. 96–103. https://doi.org/https://doi.org/10.15866/irease.v11i3.13796.

[54] Baldo, L., Bertone, M., Dalla Vedova, M. D., and Maggiore, P., "High-Fidelity Digital-Twin Validation and Creation of an Experimental Database for Electromechanical Actuators Inclusive of Failures," *2022 6th International Conference on System Reliability and Safety (ICSRS)*, IEEE, 2022, pp. 19–25. https://doi.org/https://doi.org/10.1109/icsrs56243.2022.10067403.

[55] Stevens, B. L., Lewis, F. L., and Johnson, E. N., *Aircraft control and simulation: dynamics, controls design, and autonomous systems*, John Wiley & Sons, 2015.

[56] Berri, P. C., Dalla Vedova, M. D. L., and Maggiore, P., "A smart electromechanical actuator monitor for new model-based prognostic algorithms," *International Journal of Mechanics and Control*, Vol. 17, No. 2, 2016, pp. 19–25.

[57] Berri, P. C., Dalla Vedova, M. D. L., and Maggiore, P., "Design and Development of an Electromechanical Actuator Test Bench for Validation of Health Monitoring Models," *31st European Safety and Reliability Conference*, 2021, pp. 2473–2478. https://doi.org/https://doi.org/10.3850/978-981-18-2016-8_560-cd.

[58] Sobester, A., Forrester, A., and Keane, A., *Engineering design via surrogate modelling: a practical guide*, John Wiley & Sons, 2008. https://doi.org/https://doi.org/10.2514/4.479557.

[59] Dalla Vedova, M. D. L., Berri, P. C., and Re, S., "Metaheuristic Bio-Inspired Algorithms for Prognostics: Application to On-Board Electromechanical Actuators," *2018 3rd International Conference on System Reliability and Safety (ICSRS)*, IEEE, 2018, pp. 273–279. https://doi.org/https://doi.org/10.1109/icsrs.2018.8688832.

[60] Cheng, Y., Wang, R., and Xu, M., "A combined model-based and intelligent method for small fault detection and isolation of actuators," *IEEE Transactions on Industrial Electronics*, Vol. 63, No. 4, 2015, pp. 2403–2413. https://doi.org/https://doi.org/10.1109/tie.2015.2499722.